ACS Partner Journal

CHEMICAL & BIOMEDICAL IMAGING

Open Access

pubs.acs.org/ChemBioImaging

Review

Getting the Most Out of Fluorogenic Probes: Challenges and Opportunities in Using Single-Molecule Fluorescence to Image Electro- and Photocatalysis

Meikun Shen, William H. Rackers, and Bryce Sadtler*

Cite This: *Chem. Biomed. Imaging* 2023, 1, 692−715

Read Online

ACCESS | Metrics & More | Article Recommendations

ABSTRACT: Single-molecule fluorescence microscopy enables the direct observation of individual reaction events at the surface of a catalyst. It has become a powerful tool to image in real time both intra- and interparticle heterogeneity among different nanoscale catalyst particles. Single-molecule fluorescence microscopy of heterogeneous catalysts relies on the detection of chemically activated fluorogenic probes that are converted from a nonfluorescent state into a highly fluorescent state through a reaction mediated at the catalyst surface. This review article describes challenges and opportunities in using such fluorogenic probes as proxies to develop structure−activity relationships in nanoscale electrocatalysts and photocatalysts. We compare single-molecule fluorescence microscopy to other microscopies for imaging catalysis in situ to highlight the distinct advantages and limitations of this technique. We describe correlative imaging between super-resolution activity maps obtained from multiple fluorogenic probes to understand the chemical origins behind spatial variations in activity that are frequently observed for nanoscale catalysts. Fluorogenic probes, originally developed for biological imaging, are introduced that can detect products such as carbon monoxide, nitrite, and ammonia, which are generated by electro- and photocatalysts for fuel production and environmental remediation. We conclude by describing how single-molecule imaging can provide mechanistic insights for a broader scope of catalytic systems, such as single-atom catalysts.

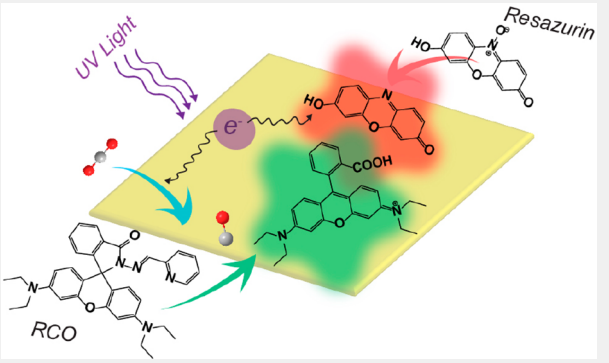

KEYWORDS: *single-molecule fluorescence, fluorogenic probes, super-resolution imaging, photocatalysis, electrocatalysis, structure−activity relationships, nanoparticles, single-atom catalysts*

INTRODUCTION

Nanoscale catalysts are being developed for a wide range of important reactions in energy conversion and storage, environmental remediation, and the production of commodity chemicals.[2−27] In these heterogeneous catalysts, the chemical reaction takes place on the surface of the material. Thus, individual steps along the reaction pathway, such as adsorption, surface diffusion, electron transfer, bond breakage, bond formation, and product desorption are highly sensitive to the surface structure of the catalyst. Different facets of a nanocrystal have different surface structures, leading to different activation energies for these steps. Surface sites with a high degree of undercoordination (i.e., a lower coordination number than the same atom would possess in the interior of the crystal) often serve as preferential reaction sites for catalysis. For example, in electrocatalysts with a layered crystal structure, such as transition metal chalcogenides, the edge atoms around the perimeter of the crystals are undercoordinated and act as preferential sites in electrocatalytic reactions, including the hydrogen evolution reaction and oxygen evolution reaction.[28−32] Crystal defects in nanoscale catalysts can also have a profound impact on their activity. For example, oxygen vacancies (i.e., the absence of an oxygen atom where it would normally be located in the crystal lattice) in semiconductor metal oxides can both enhance the concentration of photoexcited charge carriers needed for photocatalytic redox reactions and expose metal atoms at the surface that act as preferential sites for interfacial charge transfer.[33−39]

To understand the features that produce high activity and stability in nanoscale catalysts (or the lack of activity/stability), analytical methods are needed to detect reaction products and correlate the generation of those products with the structure of

Received: June 28, 2023
Revised: October 4, 2023
Accepted: October 7, 2023
Published: October 23, 2023

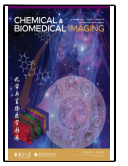

the catalyst. Common techniques to analyze the products of catalytic reactions include nuclear magnetic resonance spectroscopy, infrared spectroscopy, gas chromatography, and mass spectrometry. Combined with techniques for structural and morphological characterization, such as electron microscopy, X-ray diffraction, X-ray photoelectron spectroscopy, Raman spectroscopy, and X-ray absorption spectroscopy, these methods can provide an ensemble picture of structure−activity trends that averages over all the particles in the sample. Using these techniques, many reports have demonstrated the ability to tune the activity, selectivity, and stability of nanoscale materials for photocatalytic and electrocatalytic reactions through systematic control over the average particle morphology[29,30,40−48] and/or defect concentration.[15,16,33−39,49−51]

However, nanoscale catalysts exhibit interparticle variations that affect their activity and stability, such as differences in size, shape, surface structure, and defect concentration, even for particles synthesized within the same batch. Each particle also contains different potential reaction sites, including different crystal facets and edge sites as well as surface defects (e.g., vacancies, step edges, twin boundaries, etc.). Such heterogeneity makes it challenging to identify the actual surface sites responsible for catalytic turnovers; this critical information is averaged over when measurements are made on a large number (e.g., on the order of a mole) of catalyst particles. For example, a subpopulation of catalyst particles could be dominant in the observed ensemble activity while other particles in the batch are relatively inactive.[52−55] To make matters more complicated, the surface structures of many catalysts change when they are in their active state (i.e., catalyzing the reaction of interest).[56−59] Therefore, conventional ex-situ measurements performed before or after the reaction may not reflect the true chemical properties of the active catalyst. In-situ methods are needed to map the distribution of active regions across the surfaces of catalyst particles under conditions where they are undergoing catalytic turnovers.

Single-molecule fluorescence (SMF) microscopy provides the unique capability to probe individual chemical reactions with millisecond time resolution and nanoscale spatial resolution.[53−55,60−106] It has been used to measure both differences among the reactivity of catalyst particles prepared within the same batch and to image nanoscale variations in activity across individual particles. However, the technique relies on chemically activated fluorogenic probes that serve as proxies for the reaction of interest. The focus of this article is to describe challenges and opportunities in applying SMF imaging to understand the chemical and physical behavior of nanoscale catalysts. The examples provided in this article pertain mostly to metal and semiconductor electro- and photocatalysts that are candidates for generating useful chemical fuels through catalyzing reactions such as water splitting to produce hydrogen, the reduction of carbon dioxide into alcohols, and the reduction of nitrogen to ammonia. The article will start with a comparison of various techniques for imaging heterogeneous catalysts in their active state. We will outline the limitations of using fluorogenic probes for imaging catalytic activity via SMF microscopy and provide possible methods to overcome these limitations. Based on the current challenges and opportunities in using single-molecule fluorescence imaging, we will provide examples of catalytic systems in which this technique has the potential to provide new mechanistic insights.

A COMPARISON OF TECHNIQUES FOR IN SITU IMAGING OF HETEROGENEOUS CATALYSIS

The ideal imaging technique for revealing structure−activity trends in nanoscale catalysts would 1) determine the identities and amounts of chemical products, 2) provide atomic-level resolution of the active sites on the surface of the catalyst while it is in operation and image changes in those sites over time, 3) operate under conditions that are similar to the catalytic reaction of interest, 4) be compatible with a wide range of different catalysts and environments (e.g., in solution or the gas phase and at different temperatures and pressures), and 5) allow high-throughput screening of different catalyst compositions and structures. No current method meets all these requirements. To put the advantages (and disadvantages) of single-molecule fluorescence into context, several techniques for imaging the active regions of heterogeneous catalysts at different length scales are described below. A comparison of these different techniques is provided in Table 1.

Scanning tunneling microscopy (STM) uses a sharp tip to probe the structure of surfaces. It provides atomic resolution of catalyst surfaces and can monitor changes in their structure in situ after the introduction of gaseous species or under an applied electrochemical potential.[107−110] Differences in the adsorption, dissociation, and reactivity of molecular adsorbates such as carbon monoxide, hydrogen, and water on crystal terraces vs step edges and vacancies can be imaged.[111−114] Conformational changes in redox-active molecules can also be imaged at different applied potentials using electrochemical STM.[115−118] Moreover, when the tip of the microscope is coated with a plasmonic metal, such as Ag or Au, chemical information with nanoscale resolution can be obtained through tip-enhanced Raman spectroscopy (TERS).[119−124] So far, TERS imaging has focused on self-assembled monolayers of molecules adsorbed on metal surfaces,[119,121,124] such that the technique is limited to one catalytic turnover at each surface site unless the reactant can be regenerated in situ.[122,123] Furthermore, STM generally requires clean and nearly atomically flat surfaces (i.e., single crystals, which can be modified with clusters of metals, metal oxides, or molecular adsorbates). This restriction limits the types of catalytic systems and chemical reactions that can be studied.

While STM is well suited for imaging single-crystal surfaces, transmission electron microscopy (TEM) is better matched for imaging nanoscale catalyst particles (e.g., spherical nanoparticles, nanorods, and nanowires). The development of in situ holders for TEM in which gas and liquids can be introduced has enabled atomic-level visualization of the changes in nanoscale catalysts after reactive chemical species (e.g., H_2, O_2, or CO) are introduced into the cell.[125−129] In-situ holders designed for introducing gases are particularly useful for studying structural changes at elevated temperatures (e.g., 150 to 800 °C) during vapor-phase reactions such as methane oxidation,[130] CO oxidation,[131−133] and other reactions.[134,135] In-situ liquid-cell holders with the ability to apply an electrical bias can be used to monitor morphological changes during electrochemical processes such as lithiation/delithiation, metal dendrite formation,[136−139] and, more recently, electrochemical reactions including water oxidation and oxygen reduction.[140,141] Changes in the surface structure of photocatalyst particles, such as titanium dioxide (TiO_2), under UV irradiation and in the presence of H_2O have also been imaged.[142,143] While transmission electron microscopes can be coupled with instrumentation for detecting reaction products through mass spectrometry

https://doi.org/10.1021/cbmi.3c00075
Chem. Biomed. Imaging 2023, 1, 692−715

Table 1. Comparison of Techniques for In Situ Imaging of Heterogeneous Catalysis

Technique	Sample environment	Detection method	Characterizes	Detects reaction products?	Typical spatial resolution[a]	Typical acquisition rate[a]	Requirements/limitations
STM	Vacuum	Tunneling current	Surface structure	If adsorbed on the surface	Atomic, 0.01 nm	Scan rates vary: 0.1−100 s for a 10 × 10 nm^2 region	Requires clean, atomically flat surfaces
Gas & liquid-cell TEM	Electron-transparent cell in vacuum	Electron transmission/diffraction	Particle structure and morphology	When combined with GC or EELS	Atomic to nanoscale, 0.01−10 nm, depends on liquid thickness	8−150 frames/s for a region of 2.5 × 2.5 μm^2 (low-res) to 25 × 25 nm^2 (high-res)	Cells need high electron transparency; samples are subject to beam damage
SECM	In liquid, open to air	Electrochemical current	Charge-transfer rate	Detects rate of redox reactions	Nano- to microscale 0.05−10 μm	Scan rates vary from 30 nm/s to 10 μm/s	Primarily restricted to redox reactions
STXM	X-ray-transparent liquid cell	X-ray transmission	Distribution of elements and their oxidation states	No	Nanoscale 40−100 nm	Scan rates vary: 100 s to >1 h for a 1 × 1 μm^2 region	Requires synchrotron radiation and specialized cell design
SMF	In liquid, open to air	Fluorescence	Number of product molecules generated	If they are fluorescent	Nanoscale 10−50 nm	10−70 frames/s for an 80 × 80 μm^2 region	Requires samples and substrates with low fluorescence background

[a]The spatial resolutions and acquisition rates provided are based on representative examples. The resolution and either scan rate (for STM, SECM, and STXM) or frame rate (for TEM and SMF) will depend on the specific sample, reaction conditions, and instrument used.

(MS) or electron energy loss spectroscopy (EELS),[131,132,144−146] there is currently no way to correlate a specific region of the catalyst with the number of turnovers at that site nor how the observed structural changes affect its relative activity. So far, mapping the relative reactivity of different regions has been limited to reactions that produce gaseous products (e.g., water splitting to produce H_2 and O_2 gas) by imaging the formation of gas bubbles in liquid cells.[143,146,147] However, the gas bubbles are significantly larger (i.e., tens to hundreds of nanometers) than the reaction sites producing the bubbles. While scanning electron microscopy (SEM) does not have the atomic resolution of TEM, it can be used to image thicker samples that are not electron-transparent. Gas adsorption on metal surfaces leads to changes in the work function of the metal and corresponding changes in the brightness of the surface when imaged by SEM. This contrast mechanism has enabled observation of oscillatory dynamics for gas-phase catalytic reactions on the surface of polycrystalline metals over much larger fields of view (i.e., 500 × 500 μm^2) than can be imaged by TEM.[148]

Scanning electrochemical microscopy (SECM) maps the rates of heterogeneous charge transfer across electrode surfaces.[149−154] An ultramicroelectrode (UME) with a diameter typically ranging from several hundred nanometers to a few micrometers is scanned across the electrochemically active surface to measure current under an applied potential. The advantage of this technique is that it directly measures the rate of the electrochemical reaction of interest at a specific region (as the Faradaic current is proportional to reaction rate). Combining SECM with an illumination source, which may be coupled with the UME for localized illumination, enables scanning photoelectrochemical measurements at semiconductor electrodes.[154−158] The spatial resolution of SECM depends primarily on the diameter of the UME. While typical resolutions for this technique are hundreds of nanometers to microns, recent advances in using smaller nanoelectrodes for SECM have provided spatial resolutions of 15 to 55 nm,[157,159,160] which is comparable to that obtainable by single-molecule fluorescence imaging. A variant of SECM is scanning electrochemical cell microscopy (SECCM), where, instead of immersing the entire sample in an electrolyte solution, a pipet probe containing both the counter and reference electrodes is scanned across the sample surface with a drop of electrolyte between the scanning probe and the sample.[156,161−164] In this case, the resolution is determined by the size of the liquid droplet and can vary from hundreds of nanometers to microns. As will be discussed in more detail for the case of SMF imaging below, understanding structure−activity relationships in catalysts using SECM often requires correlating the resulting current maps with other techniques such as electron microscopy or Raman microscopy to examine the morphology and/or structure of the area imaged.[153,158,165−167]

Scanning transmission X-ray microscopy (STXM) uses a focused and coherent X-ray beam from a synchrotron source to image the transmission of X-rays through the catalyst sample.[168−170] By tuning the X-ray energy to match the absorption edge of a specific electronic transition for an element, this technique enables nanoscale chemical mapping of the local oxidation state of that element in the catalyst.[171−178] The distribution of different elements in the sample can be obtained by imaging with multiple X-ray energies. Typical spatial resolutions for in situ STXM are 40 to 100 nm, although resolutions below 10 nm have been obtained for ex situ

https://doi.org/10.1021/cbmi.3c00075
Chem. Biomed. Imaging 2023, 1, 692−715

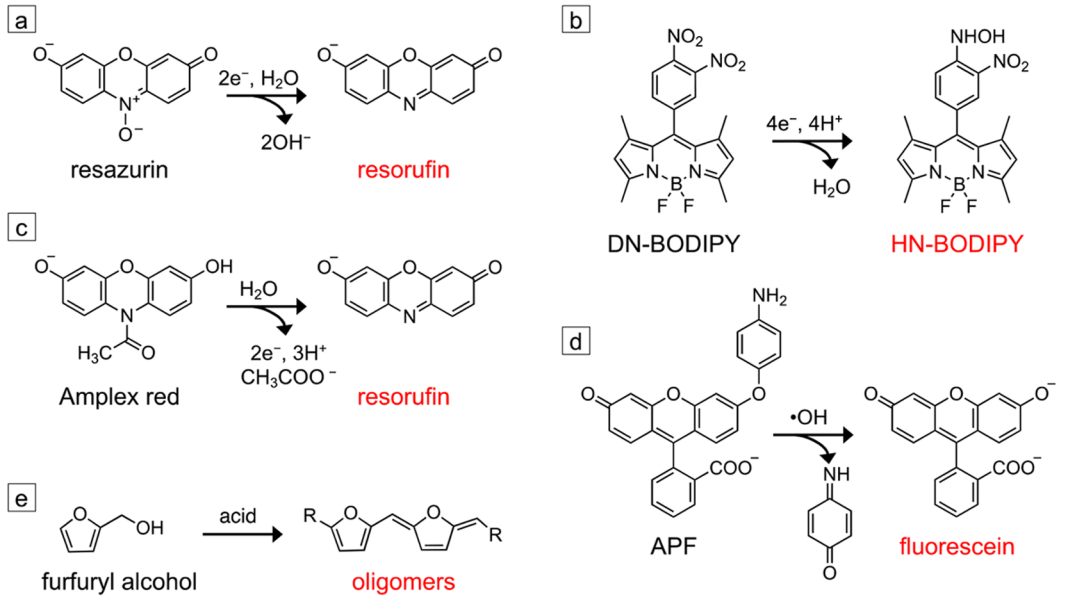

Figure 1. Fluorogenic probes used for SMF imaging of nanoscale catalysts. (a) Reductive N-deoxygenation of resazurin produces fluorescent resorufin. (b) The reduction of the *para*-nitro group of 8-(3,4-dinitrophenyl)-1,3,5,7-tetramethyl-4,4-difluoro-4-bora-3a,4a-diaza-*s*-indacene (DN-BODIPY) into a hydroxylamino group produces the fluorescent HN-BODIPY. (c) Oxidative N-deacetylation of Amplex red produces resorufin. (d) Oxidative cleavage of the aminophenyl group of 3′-(*p*-aminophenyl) fluorescein (APF) produces fluorescein. Both Amplex red and APF can either be directly oxidized by the catalyst to produce the fluorescent product, or they can be activated by reactive oxygen species generated at the catalyst surface. (e) The acid-catalyzed condensation of furfuryl alcohol produces fluorescent oligomers. All probes except the one shown in panel (b) are commercially available. The synthesis of the DN-BODIPY probe is described in ref 187.

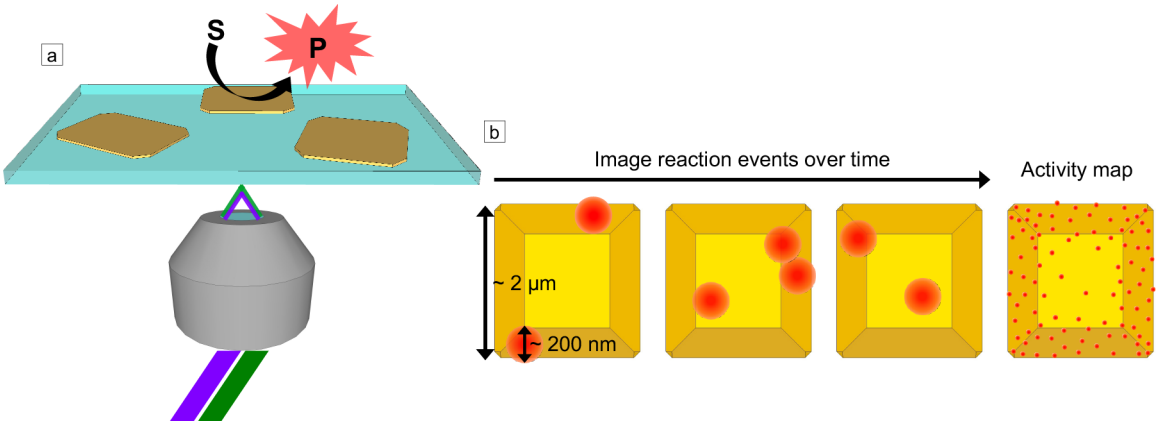

Figure 2. Single-molecule fluorescence imaging of fluorogenic probes on nanoscale catalysts. (a) Schematic of objective-based TIRF microscopy in which a laser is sent through a TIRF microscope objective at an angle such that it is internally reflected by the glass coverslip. The catalyst converts an initially nonfluorescent substrate molecule (S) into a fluorescent product (P). The evanescent field from the TIRF illumination excites the fluorescent product, and photons emitted by the activated probe are collected by the objective. For semiconductor photocatalysts, dual excitation may be used in which one laser with a photon energy greater than the band gap of the semiconductor (e.g., 405 or 450 nm) excites electrons into the conduction band of the semiconductor, and a lower-energy laser (e.g., 488, 532, or 567 nm) excites the activated probe. (b) Schematic for superlocalization of activated probe molecules (red circles) on a faceted catalyst particle (shown in yellow). The emission profile for each fluorescent molecule is diffraction-limited, but the center position of the fluorophore can be localized with nanoscale precision given a sufficient number of photons are collected over the background and as long as two molecules within a diffraction-limited region are not emitting at the same time. By localizing the positions of many activated probes over time, super-resolution activity maps can be produced, which show how the activity varies at the nanoscale across the catalyst surface (right image in panel b).

STXM.[179] STXM enables the acquisition of highly multiplexed data sets where the evolution of the oxidation states of different elements and their distribution can be mapped as a function of electrochemical potential, temperature, or reactive gas pressure.[171−177] Thus, differences in the local chemical composition of the catalyst can be compared when it is in its active vs inactive states. Similar to in situ TEM, STXM cannot measure the local activity of the catalyst. For electrocatalysts, STXM images have been correlated with SECM maps to understand how the local oxidation state of elements in the sample mediate the resulting electrocatalytic current.[171]

Imaging catalysis at the nanoscale with single-molecule fluorescence relies on chemically activated fluorogenic probes. These probes are initially nonfluorescent but are converted into

https://doi.org/10.1021/cbmi.3c00075
Chem. Biomed. Imaging 2023, 1, 692−715

a highly fluorescent state through a reaction catalyzed at the catalyst surface. Figure 1 provides examples of common fluorogenic probes used for imaging reduction, oxidation, and acid-catalyzed reactions. As this review focuses on heterogeneous catalysis, we will primarily discuss probes that undergo irreversible chemical reactions that activate them into their fluorescent state. Fluorogenic probes that reversibly interconvert between their nonfluorescent and fluorescent states through changes in pH and/or temperature[180−182] or an applied electrical bias[183,184] are used in other SMF imaging techniques. Once activated, individual fluorescent probes can be detected using fluorescence microscopy, allowing single-turnover counting of the reaction events that occur on the catalyst surface.

Different illumination geometries can be used for exciting the activated probes. A common geometry depicted in Figure 2a is objective-based total internal reflection fluorescence (TIRF) microscopy in which laser illumination enters a microscope objective at an angle. The critical angle, θ_C, for total internal reflection of incident light within the microscope coverslip is given by $\sin(\theta_C) = n_2/n_1$, where n_1 is the refractive index of the coverslip and n_2 is the refractive index of the solution above it. For an aqueous solution in which $n_2 \approx 1.33$ and $n_1 = 1.5$ for the glass coverslip, then $\theta_C = 62.5°$. When the angle is adjusted to be greater than θ_C, the incident laser light is totally internally reflected within the glass coverslip on which the catalyst sample has been deposited, and an evanescent excitation field is created. The evanescent field formed by TIRF excitation extends several hundred nanometers into the sample volume above the coverslip and can be tuned with the wavelength and incident angle of the laser excitation.[185,186]

The chemical transformation that activates the fluorogenic probe at the surface of the catalyst occurs much faster (i.e., subpicosecond time scale) than the typical camera exposure times of 15 to 100 ms used for SMF imaging. Thus, the activated probe molecule appears as a sudden increase in fluorescence intensity between imaging frames and has a diffraction-limited emission profile (Figure 2b). The activated probe can turn off through different mechanisms including desorption from the surface, photobleaching, or undergoing further conversion to a nonfluorescent product. When a fluorescent probe leaves the surface of the catalyst, it is no longer observed as its diffusion in solution is much faster than the typical exposure times of the camera. Thus, each reaction event appears as a fluorescence burst during imaging. Since the bulk imaging solution is not excited by the evanescent field, TIRF excitation significantly reduces solution background fluorescence relative to epifluorescence excitation (from either activated probe molecules once they diffuse into the bulk solution or from probes that are weakly fluorescent in their initial inactive state). The microscope objective collects photons emitted from activated probes, and an electron-multiplying charge-coupled device (EM-CCD) camera with high quantum efficiency is typically used for imaging.

Detecting individual fluorescence bursts from activated probes provides the ability to perform super-resolution imaging to observe variations in catalytic activity below the diffraction-limited resolution of an optical fluorescence microscope. Localizing the centroid position of each fluorescence burst (i.e., reaction event) relies on fitting the emission profile of the probe, which spreads over several pixels of the EM-CCD camera (see the inset in Figure 3a for an example). A Gaussian function is typically used for fitting the emission profile of a single fluorophore. However, for fluorescent molecules coupled to plasmonic metal nanostructures (which can serve as photocatalysts), other fitting functions may be necessary.[188−191] The localization precision in SMF imaging increases with the signal-to-noise ratio of the number of photons emitted by the fluorophore over the background photons and is typically in the range of 10 to 50 nm for SMF imaging of nanoscale catalysts. For example, our research group typically achieves a localization precision between 25 and 30 nm when applying this technique to semiconductor photocatalysts, such as tungsten oxide and bismuth oxybromide.[55,81−83] This spatial resolution is comparable to that obtained by other SMF techniques used for biological specimens such as photoactivated localization microscopy (PALM) and stochastic optical reconstruction microscopy (STORM).[192−196] By counting reaction events one-by-one, super-resolution activity maps are generated, which

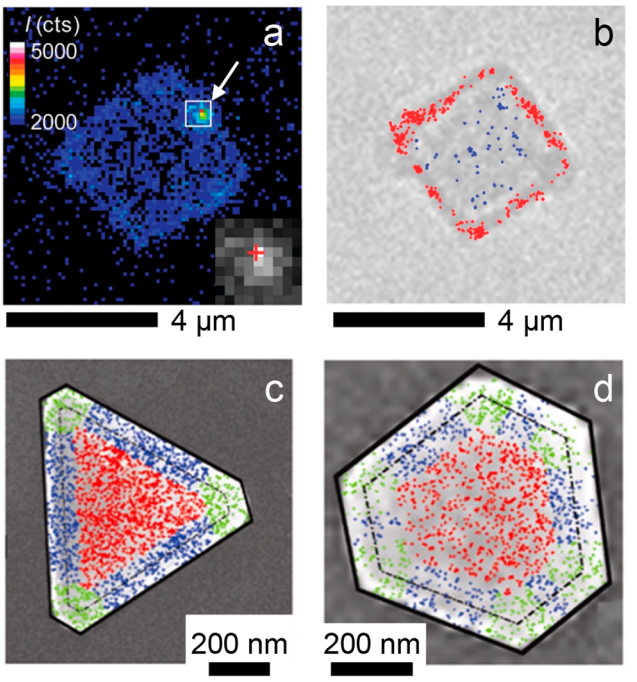

Figure 3. Correlating SMF activity maps with optical and electron microscopy images. (a) Frame from SMF imaging showing a fluorescence burst (indicated by the white arrow) due to the photocatalytic reduction of DN-BODIPY on the surface of a TiO_2 microcrystal. The color scale represents the fluorescence intensity counts. The inset shows an expanded view of the fluorescence burst, whose emission profile spreads over several pixels of the EM-CCD camera. (b) Optical transmission microscopy image of the same TiO_2 microcrystal. The red dots indicate activated HN-BODIPY probes localized on the {101} facets around the perimeter of the microcrystal, while the blue dots indicate activated probe molecules localized on the basal {001} facet. The scale bars below each image are 4 μm. Panels (a) and (b) are adapted with permission from ref 87. Copyright 2011 American Chemical Society. (c) Activity map for the reduction of resazurin to resorufin on a triangular Au nanoplate overlaid on an SEM image of the same nanoplate. 2325 fluorescence bursts were localized to generate the activity map. The fluorescence bursts are color-coded to indicate different regions of the nanoplate with bursts from the flat {111} facet in red, bursts near the edges of the nanoplate in blue, and bursts near the corners in green. The dashed black line outlines the perimeter of the Au nanoplate, and the solid black line outlines the mesoporous silica shell coating the Au nanoplate. (d) Same as (c) but for a different hexagonal Au nanoplate with 1579 fluorescence bursts detected. The scale bars below each image are 200 nm. Panels (c) and (d) are adapted with permission from ref 80. Copyright 2013 American Chemical Society.

https://doi.org/10.1021/cbmi.3c00075
Chem. Biomed. Imaging 2023, 1, 692−715

quantify how the number of catalytic turnovers varies at the nanoscale across the surface of the catalyst (Figure 2b). Because the imaging technique uses widefield optical microscopy, many particles can be imaged simultaneously, enabling quantification of heterogeneity in the reactivity of different catalyst particles synthesized within the same batch.[88,197,198]

In addition to nanoscale spatial resolution, SMF microscopy can quantify reaction kinetics on individual catalyst particles through statistical analysis of the fluorescence bursts. The individual off times, τ_{off}, between fluorescence bursts and on times, τ_{on}, for fluorescence bursts are stochastic. However, the inverse of the average values of these parameters, $\langle\tau_{off}\rangle^{-1}$ and $\langle\tau_{on}\rangle^{-1}$, can be related to kinetic and thermodynamic parameters such as the rate constant for product formation, the equilibrium constant for adsorption of the probe on the surface of the catalyst, and the rate constant for dissociation of the activated probe.[53] Determining these parameters for different catalyst particles requires an appropriate model for the reaction. The most common model used in SMF imaging is the Langmuir–Hinshelwood mechanism for surface reactions in which the adsorption of the fluorogenic probe is fast relative to its subsequent conversion into the activated product:[53,65,73,82,83,85−87,90,99]

$$\nu = \langle\tau_{off}\rangle^{-1} = \frac{\gamma_{eff}K_{ad}[S]}{1 + K_{ad}[S]}$$

In this equation, ν is the turnover rate, γ_{eff} is the effective rate constant for activation of the probe, K_{ad} is the equilibrium constant for adsorption of the probe onto the surface of the catalyst, and $[S]$ is the concentration of the fluorogenic probe in solution. Fitting this equation is normally done on a per particle basis such that γ_{eff} combines all reaction sites on the catalyst particle. Differences in γ_{eff} for different catalyst particles indicate differences in either the number of active sites or their intrinsic activity. It is common in the literature of SMF imaging of heterogeneous catalysts to either use the inverse of the average off time, $\langle\tau_{off}\rangle^{-1}$, to calculate the turnover rate, ν, or to count the number of fluorescence bursts observed over a given time period. When ν is divided by the surface area of the catalyst, it gives the specific activity. The dependence of the inverse of the average on time, $\langle\tau_{on}\rangle^{-1}$, on the concentration of the probe provides information on how the probe desorbs from the surface of the catalyst.[53] When $\langle\tau_{on}\rangle^{-1}$ is independent of $[S]$, it indicates that the activated probe undergoes self-dissociation from the catalyst surface. On the other hand, when $\langle\tau_{on}\rangle^{-1}$ depends on $[S]$, it indicates that self-dissociation competes with substrate-assisted dissociation.

SMF microscopy can also be used to image changes in the activity of the catalyst in situ. While the time resolution for imaging a single burst is milliseconds (based on the exposure time of the camera), many reaction events need to be detected to perform statistical analysis of the on and off times of fluorescence bursts or to compare activity maps collected over different time periods. While the types of dynamic processes that can be observed depend on the specific catalyst, the probe used, and the reaction conditions, we describe some representative examples. When monitoring the activity of catalyst particles that are smaller than the localization precision of individual fluorophores, such as metal nanoparticles with diameters less than 20 nm, the concentration of the fluorogenic probe needs to be low enough such that one activation event occurs at a time on each particle (i.e., one probe turns off before the next one turns on). By imaging hundreds of fluorescence bursts for the reduction of resazurin or the oxidation of Amplex red on individual Au, Pt, or Pd nanoparticles over periods of hundreds to thousands of seconds, fluctuations in the frequency of reaction events are frequently observed.[53,65,66,92] These variations have been attributed to a combination of catalysis-induced restructuring of the surface of the metal nanoparticles as well as spontaneous surface restructuring.

For spatial mapping of the activity of larger catalyst particles (e.g., microcrystals, nanoplates, and nanorods), the separation between activated probes in each frame should be larger than their diffraction-limited emission profiles. For example, we imaged changes in the photocatalytic activity of bismuth oxybromide (BiOBr) nanoplates for the reduction of resazurin.[82] We compared activity maps acquired for 2500 frames with a 50 ms exposure time (i.e., 2.08 min) over a period of 32 min. Photoinduced increases in the concentrations of crystal defects in the BiOBr nanoplates (i.e., Bi ions in a reduced oxidation state and oxygen vacancies) led to increased activity in individual nanoplates during the first 5 min followed by a slow decrease in activity. Alivisatos and co-workers mapped the activity of a single antimony-doped TiO_2 nanorod for the photocatalytic oxidation of Amplex red.[89] Over a period of 13 h, they detected ∼10,000 reaction events on the surface of the nanorod. By creating a series of activity maps that each included ∼2000 events, they observed time-dependent spatial variations in activity. During the first 3 h of observation, the majority of reaction events occurred near the middle of the TiO_2 nanorod; at later times, the fluorescence bursts transitioned to occur primarily near the ends of the nanorod.

Comparing the different microscopy techniques discussed above (STM, TEM, SECM, STXM, and SMF), STM and TEM provide the highest resolution for imaging structural changes in nanostructured catalysts when they are in their catalytically active state. However, the requirement for a high-vacuum chamber (even if the sample itself is in a liquid cell inside the vacuum chamber) restricts the types of samples that can be imaged by these techniques and makes them relatively low-throughput. Furthermore, TEM and STM do not measure variations in catalytic turnovers across different regions of the sample. STXM has lower resolution than STM or TEM, but it can measure the spatial distribution of elements and their oxidation states at the nanoscale when the catalyst is in its active state. Furthermore, due to the higher penetration depth of X-rays relative to electrons, thicker samples (i.e., thicknesses >1 μm) can be imaged using STXM compared with TEM. Both in situ TEM and STXM require specialized reactor cells that are electron- or X-ray-transparent, respectively. Furthermore, STXM requires a synchrotron facility to generate the X-rays. While SECM and SMF do not provide atomic resolution of the catalyst structure, they can quantify reaction kinetics at the nano/microscale across the surface of the catalyst. They can be performed under conditions relevant to electrochemical and photochemical energy conversion (e.g., with the sample in aqueous solution open to air). SECM and SMF are also well suited for observing changes in the response of a catalyst under different chemical conditions (e.g., pH or concentration of the reactant) and physical stimuli (e.g., light intensity or applied potential). In comparing SECM to SMF, the main advantage of SECM is that it directly provides rates for electrocatalytic reactions of interest (e.g., the hydrogen evolution reaction or oxygen evolution reaction), whereas SMF relies on chemically activated fluorogenic probes as proxies for catalytic activity. A

https://doi.org/10.1021/cbmi.3c00075
Chem. Biomed. Imaging 2023, 1, 692−715

significant difference between the two techniques is that SECM measures the products of the electrochemical reaction at a distance that is determined by the separation between the UME and the sample surface. Thus, the measured current convolves the generation of chemical products with their diffusion, which can make analysis more difficult (i.e., a model is needed to relate time-dependent concentration profiles to the measured current). In single-molecule fluorescence using TIRF microscopy, activated fluorogenic probes are detected at the catalyst surface and are no longer observed once they diffuse away. The main advantage of SMF microscopy over SECM is the higher spatial resolution. While sub-100 nm resolution can be achieved by SECM, the resolution is typically much lower (i.e., several hundred nanometers to several microns). SMF imaging can routinely achieve a resolution of 10 to 50 nm. This higher spatial resolution is critical to achieve the super-resolution activity maps described in the next section.

CHALLENGES AND POTENTIAL SOLUTIONS IN APPLYING SINGLE-MOLECULE FLUORESCENCE TO HETEROGENEOUS CATALYSIS

Pioneering studies in SMF imaging of heterogeneous catalysis focused on model systems including zeolite microcrystals,[60−63] gold and platinum nanoparticles,[53,64−66] and the photocatalytic generation of reactive oxygen species by TiO_2 microcrystals.[67−69] Over the last 18 years, this technique has expanded to more complex catalytic systems and has enabled visualization of nanoconfinement in porous catalysts,[70−72] photoexcited charge flow in semiconductor−semiconductor and semiconductor−metal heterostructures,[73−79] and nonuniform activity in metal and semiconductor catalysts due to nanoscale spatial variations in their defect concentration.[54,55,80−84] Many of these papers use the fluorogenic probes shown in Figure 1. Resazurin (Figure 1a)[53,55,64−66,76,79,80,82,85,88−90,92−94,97,99,100] and 8-(3,4-dinitrophenyl)-1,3,5,7-tetramethyl-4,4-difluoro-4-bora-3a,4a-diaza-*s*-indacene (DN-BODIPY) (Figure 1b)[73,74,87] can be used to image reduction reactions, while Amplex red (Figure 1c)[54,66,70−72,75−79,86,88,89,94,96,97,100] and 3′-(*p*-aminophenyl) fluorescein (APF) (Figure 1d)[55,69,81,83,84,186] can be used to image oxidation reactions. Furfuryl alcohol condenses in the presence of acid to form fluorescent oligomers (Figure 1e), which can be catalyzed by solid acid catalysts such as zeolites or tungsten oxide.[61,62,81,83]

It is important to consider the compatibility of these probes with the reaction conditions employed for heterogeneous catalysis. For example, the photocatalytic reduction of resazurin to resorufin has been shown to be inhibited by oxygen.[76,199] Furthermore, the fluorescence intensity of resorufin has a strong pH dependence. The pK_a of resorufin in near 6, and the fluorescence intensity rapidly rises above this pH.[200] Resazurin is typically used in aqueous solutions but can also be activated to resorufin in organic solvents including ethanol, acetone, and dimethyl sulfoxide (DMSO).[201] While the initial reduction of resazurin to resorufin is irreversible, resorufin can be reversibly reduced to dihydroresorufin, which is colorless and nonfluorescent. Thus, additional control experiments are needed when using resazurin as a probe for reduction reactions to determine whether the turn-off events for individual fluorescent bursts are due to the desorption of resorufin from the surface of the catalyst or its further reduction to dihydroresorufin.[82,85]

Similar to resazurin, the initial reduction of the *para*-nitro group of DN-DODIPY to a hydroxylamino group produces highly fluorescent HN-BODIPY (Figure 1b). Further reduction of the hydroxylamino group to an amine makes the probe weakly fluorescent.[187] While SMF imaging of TiO_2 photocatalysts with DN-BODIPY was done in methanol as this probe is not soluble in water, Majima and co-workers also synthesized a sulfonated version of the probe that is water-soluble.[74] In general, BODIPY dyes can be designed to be soluble in solvents spanning a wide range of polarities from water to nonpolar organic solvents. As described further below, Chang and co-workers developed a BODIPY-based probe for detecting carbon monoxide that they tested in both methylene dichloride and buffered aqueous solutions (pH 7.4).[202] Blum and co-workers have developed BODIPY-based fluorescent tags for single-molecule imaging of polymerization reactions that are soluble in organic solvents commonly used for polymerization (e.g., toluene and heptane).[52,104,203−205]

Amplex red, which can be oxidized to fluorescent resorufin (Figure 1c), exhibits only partial solubility in water. When used in biological assays to detect hydrogen peroxide (H_2O_2), it is first dissolved in DMSO and then diluted with water.[200,206] While Amplex red is more commonly used for the detection of H_2O_2, the presence of DMSO would inhibit its activation by catalysts that generate hydroxyl radicals ($^{\bullet}OH$) as DMSO is a scavenger for $^{\bullet}OH$. Amplex red slowly degrades in the presence of oxygen, and it is unstable at pH values above ∼8.5.[200,207] Combining the pH-dependence of the fluorescence intensity of resorufin and the stability of Amplex red, the usable pH range for this probe is approximately between 7 and 8.5. Finally, following the oxidation of Amplex red to resorufin, it can be further oxidized to nonfluorescent resazurin, which again necessitates control experiments to determine the mechanism of turn-off events during SMF imaging.

We have found APF to be more stable than Amplex red against oxidative degradation during long-term storage of the probes. We typically store Amplex red as a dry powder at −20 °C and APF as a solution in dimethylformamide (DMF) at 4 °C. APF also exhibits higher selectivity for activation by more reactive oxygen species. It can be activated into its fluorescent state (i.e., fluorescein) by $^{\bullet}OH$ and hypochlorite (OCl^-), but unlike Amplex red, it is not activated by H_2O_2 or superoxide anion radicals ($^{\bullet}O_2^-$).[208] Similar to Amplex red, APF is typically first dissolved in DMF (rather than DMSO) and then diluted with water. For SMF imaging of semiconductor photocatalysts including TiO_2, tungsten oxide, and indium selenide, APF has been used in aqueous phosphate buffer solutions at pH 7.4.[55,81,83,84,186]

Whereas nanomolar to micromolar concentrations are typically used for the other fluorogenic probes described above, SMF imaging with furfuryl alcohol has been performed in a 10% solution (by volume) of furfuryl alcohol in either water or dioxane.[61,62,81,83] At the ensemble level, the rate of the condensation reaction exhibits a strong solvent dependence; solvents that inhibit the formation of a carbocation intermediate lead to lower reaction rates.[209] The condensation of furfuryl alcohol also produces a variety of different fluorescent oligomers.[210,211] Using water as the solvent, we found that these products become insoluble as the chain lengths of the oligomers increase. The oligomers eventually stick to the surface of the catalyst, which limits SMF imaging with furfuryl alcohol to a few minutes.

When using the probes described above (Figure 1), many reports have observed variations in activity across the surface of individual particles.[54,55,60−63,73−76,78−84,87,89,93,96,97,100] However, SMF imaging does not directly report on the structural

https://doi.org/10.1021/cbmi.3c00075
Chem. Biomed. Imaging 2023, 1, 692−715

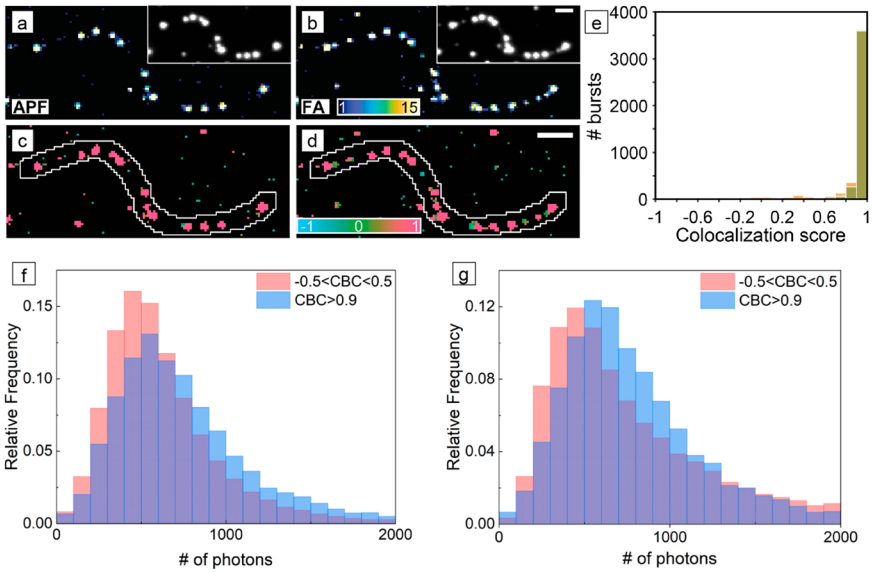

Figure 4. Spatial colocalization of different fluorogenic probes during SMF imaging. (a, b) Super-resolution activity maps of the same $W_{18}O_{49}$ nanowire for (a) the photocatalytic oxidation of APF and (b) the acid-catalyzed condensation of furfuryl alcohol (FA). The color scale provides the number of fluorescence bursts per 120 nm × 120 nm bin. The insets show the diffraction-limited image prior to localization of individual fluorescent bursts. (c, d) Coordinate-based colocalization (CBC) maps for fluorescence bursts using (c) APF and (d) FA. The color scale provides the median colocalization score of the bin, which ranges from −1 for anticorrelated to +1 for perfectly correlated. Scale bars are μm. (e) Distributions of CBC scores for individual fluorescence bursts on the nanowire from the activation of APF (green) and FA (orange). Panels (a) through (e) adapted with permission from ref 81. Copyright 2020 American Chemical Society. (f, g) Distributions of the number of photons detected per localization during (f) the photocatalytic oxidation of APF and (g) the photocatalytic reduction of resazurin during SMF imaging of BiOBr nanoplates. The blue histograms in panels (f) and (g) are localizations that had CBC scores greater than 0.9, which indicate that the oxidation and reduction reactions were colocalized in that region of the nanoplate. The red histograms in panels (f) and (g) are localizations that had CBC scores between −0.5 and 0.5, which indicate spatially uncorrelated activity for the two probe reactions. Panels (f) and (g) adapted with permission from ref 55. Copyright 2021 American Chemical Society.

or chemical features that lead to these variations in activity. As described further below, corner atoms in faceted metal nanocrystals, oxygen vacancies in metal oxide semiconductors, and individually dispersed metal atoms in single-atom catalysts can all serve as preferential reaction sites for catalysis. The nanoscale resolution (e.g., 10 to 50 nm) provided by this technique is larger than the atomic scale of these individual reaction sites. Thus, correlating activity maps obtained from SMF imaging with the nature of active sites remains a critical challenge. Based on these limitations, two fundamental questions that we are frequently asked are 1) What can imaging fluorogenic probes tell you about the chemical nature of active sites in the catalyst? and 2) How well do the probes predict activity trends for industrially relevant catalytic reactions (e.g., for the production of fuels or commodity chemicals)? In the rest of this section, we try to answer these questions and propose solutions to overcome the limitations described above.

Performing correlative SMF imaging with other microscopies (e.g., optical or electron microscopy) on the same catalyst particles has been used to connect morphological features with observed variations in activity. Majima and co-workers correlated SMF images of TiO_2 microcrystals for the photocatalytic reduction of DN-BODIPY to HN-BODIPY with optical transmission images of the same microcrystals (Figure 3a, b). They demonstrated that the reduction of DN-BODIPY occurs preferentially at the {101} facets of the TiO_2 microcrystals compared with the {001} facets.[87,187] They proposed that photoexcited electrons, whether generated at the {001} or {101} facets, are preferentially extracted from {101} facets due to a lower conduction band energy (i.e., further from the vacuum level) for the {101} facets.

Chen and co-workers correlated SMF activity maps of Au nanoplates coated with a mesoporous silica shell with scanning electron microscopy (SEM) images of the same particles (Figure 3c, d).[80] The Au nanoplates exhibited the highest specific activity (as determined by counting the number of activated probes per unit time and per lateral area) for catalyzing the reduction of resazurin to resorufin (using hydroxylamine as the reductant) at nanoscale regions near the corners of the nanoplates. The activity was lower near the edges and lowest within the {111} facets that make up the basal surfaces of the nanoplates. These morphological differences in activity can be rationalized by the different coordination numbers of Au atoms at the corners, edges, and basal facets. Au atoms within the interior of a face-centered cubic crystal have a coordination number of 12. At a perfectly flat {111} facet, the coordination number will be 9. The coordination number of Au atoms is lower at edges of the crystal where two facets meet and even lower at corners where three or more facets meet. A lower coordination number for atoms at the surface of a metal catalyst can strengthen interactions with adsorbed substrate molecules, which explains the observed activity trend. Interestingly, even within the {111} basal facet, a radial gradient in activity was observed; the activity was higher near the center of the nanoplate and lower near the periphery. The authors proposed that within a {111} facet, there is a radial gradient in the density of surface defects that is highest at the center of the Au nanoplate where nucleation and growth of the colloidal particle initiate.

https://doi.org/10.1021/cbmi.3c00075
Chem. Biomed. Imaging 2023, 1, 692−715

As the example above shows, surface defects within a single facet can act as preferential reaction sites. However, SEM is not capable of resolving such surface defects in nanoscale catalyst particles. Thus, methods are needed to correlate the locations of these defects with SMF activity maps. Ideally, high-angle annular dark-field scanning transmission electron microscopy (HAADF-STEM) could be used to image individual point defects in the crystals and correlate the locations of those defects with SMF activity maps. So far, correlative studies between SMF images and TEM images have been limited.[212] One persisting challenge is finding a substrate that is compatible with both imaging techniques (i.e., is electron-transparent and will not lead to fluorescence quenching of the fluorogenic probes).

While a single fluorogenic probe does not provide direct chemical information on the nature of active regions, performing SMF imaging using two complementary probes that are activated by different mechanisms can narrow down the potential surface sites responsible for the observed activity maps. Several reports have compared how the same catalyst can exhibit different activities for the reduction of resazurin and oxidation of Amplex red.[66,88,94] In semiconductors like TiO_2 and bismuth vanadate ($BiVO_4$), these probes are activated at different regions of the particle (e.g., different crystal facets), indicating different surface sites are responsible for the extraction of photogenerated electrons and holes.[76,79,97,100] Tailoring the structure of the fluorogenic probe can also provide information on how it interacts with the surface of the catalyst. For example, Hofkens and co-workers compared different fluorescein derivatives that were activated by transesterification on the surface of a lithium−aluminum-layered double-hydroxide microcrystal.[60] Adding a negatively charged carboxylate group to the fluorescein derivative increased the rate of its activation due to stronger adsorption of the probe on the surface of the positively charged microcrystal.

We have used the spatial correlation between different fluorogenic probes to understand how the nonuniform distribution of oxygen vacancies, a common defect in metal oxide semiconductors, controls spatial variations in their photocatalytic activity.[55,81,83] In collaboration with Lew and co-workers, we developed a coordinate-based colocalization algorithm to quantify the spatial correlation between two data sets of single-molecule localizations.[81] For example, tungsten oxide with the $W_{18}O_{49}$ monoclinic phase is a semiconductor that is active for the photocatalytic oxidation of water to oxygen. Under illumination, photoexcited holes first oxidize water to generate hydroxyl radicals as an intermediate toward further oxidation to O_2. We used APF to image the photocatalytic generation of $^{\bullet}OH$ radicals on the surface of $W_{18}O_{49}$ nanowires (in which potassium iodate was used as a scavenger for photoexcited electrons to maintain charge balance). We observed that the nanowires exhibited significant variations in activity along their lengths with hot spots of high specific activity interspersed with inactive regions (Figure 4a). As metal ions exposed by surface oxygen vacancies can act as preferential reaction sites for water oxidation to generate $^{\bullet}OH$,[37,38] we hypothesized that the variations in activity were related to variations in the concentration of oxygen vacancies along the nanowires. We then imaged the same $W_{18}O_{49}$ nanowires using furfuryl alcohol (FA) to map the distribution of acidic sites along their lengths (Figure 4b). While both surface hydroxyl groups (i.e., Bronsted acid sites) and oxygen vacancies (i.e., Lewis acid sites) can catalyze the condensation of FA to produce fluorescent oligomers, we performed SMF imaging at a pH of 7.4 such that the surface hydroxyl groups would be deprotonated for this metal oxide (which has a point of zero charge near a pH of 0.43). Thus, oxygen vacancies are the primary surface site on $W_{18}O_{49}$ nanowires responsible for the activation of FA. Using the coordinate-based colocalization (CBC) algorithm, each fluorescence burst is assigned a score based on its spatial proximity to bursts from the other probe reaction. In the colocalization maps in Figure 4c, d, red regions indicate segments of the nanowire where the activation of both APF and FA take place. Only APF activation occurs in blue-green regions in the colocalization map in Figure 4c, while only FA activation occurs in blue-green regions in the colocalization map in Figure 4d. As oxygen vacancies are the only surface site that can activate both fluorogenic probes, the high spatial correlation between the two reactions (Figure 4e) in which most segments along the nanowires either are active for both reactions or are completely inactive revealed that the distribution of oxygen vacancies is nonuniform along the nanowires. Colocalization analysis indicates that nanoscale regions containing high concentrations of oxygen vacancies serve as the active sites for photocatalysis in this metal oxide.

Introducing species that block active sites on the surface of the catalyst or compete with the fluorogenic probe for catalytic turnovers can also provide knowledge on the chemical nature of active regions. For example, we coated the surface of the $W_{18}O_{49}$ nanowires described above with polyvinylpyrrolidone, PVP, a polymer commonly used in the synthesis and processing of metal and metal oxide nanocrystals. PVP both reduced the activity of the nanowires for the activation of APF and reduced the spatial colocalization of regions that activated both APF and FA.[81] The changes in the activity maps indicated that the polymer blocked catalytic sites where the generation of $^{\bullet}OH$ radicals occurred. Calculations using density functional theory suggested that PVP coordinates to surface tungsten ions exposed by oxygen vacancies, which would prevent these sites from binding hydroxide ions to produce $^{\bullet}OH$ radicals via transfer of photogenerated holes from the semiconductor. Thus, understanding how PVP interacted with the surface of $W_{18}O_{49}$ provided further support that surface oxygen vacancies were the active sites in the initial, uncoated nanowires.

Chen and co-workers demonstrated how surface processes involving nonfluorescent species could be evaluated during SMF imaging through their competition with the activation of a fluorogenic probe.[96,98] They imaged the photoelectrochemical oxidation of Amplex red to resorufin on the surface of faceted $BiVO_4$ microcrystals.[96] By titrating increasing amounts of a reducing agent, hydroquinone (which is oxidized to 1,4-benzoquinone), they quantified how the adsorption of hydroquinone on different facets of the $BiVO_4$ microcrystals affected the number of turnovers imaged for the oxidation of Amplex red. A more significant drop in reaction events on the basal {010} facets indicated that hydroquinone adsorbed more strongly to these facets relative to the {110} facets around the perimeter of the microcrystals.

Differences in the intensities of fluorescence bursts can also provide information on the chemical nature of active sites. When performing SMF imaging of semiconductor photocatalysts, our group has employed fluorogenic probes that emit at a lower energy (i.e., longer wavelength) than the band gap energy of the semiconductor. For example, fluorescein generated by the oxidation of APF has an emission maximum near 517 nm, while resorufin generated by the reduction of resazurin or oxidation of Amplex red has an emission maximum near 583 nm. Samples of

https://doi.org/10.1021/cbmi.3c00075
Chem. Biomed. Imaging 2023, 1, 692−715

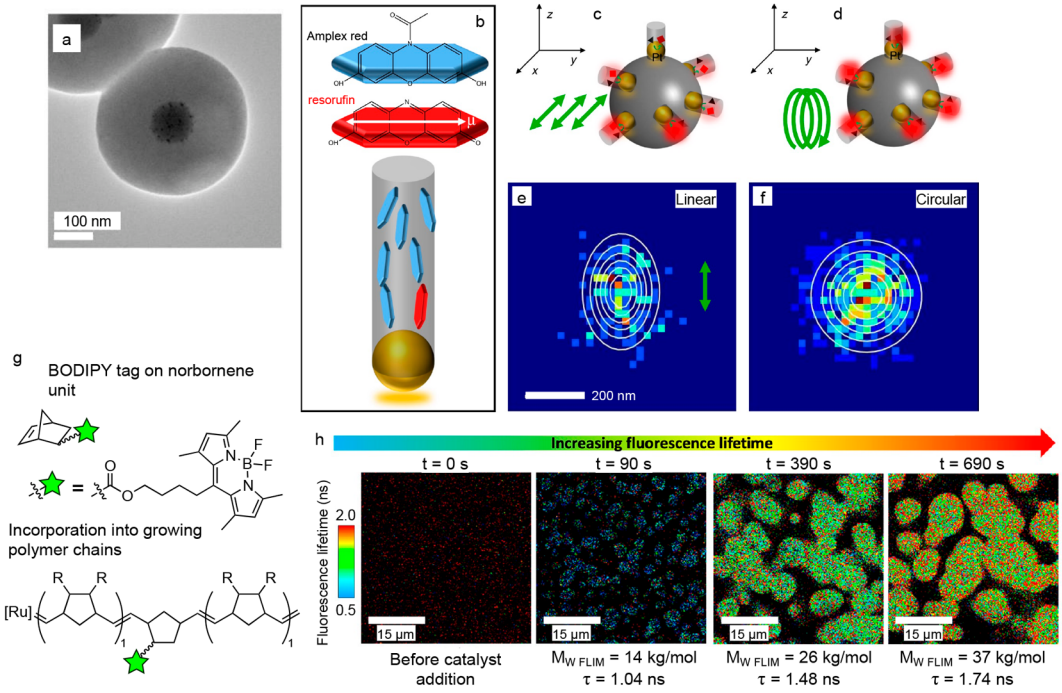

Figure 5. Measuring the polarization and lifetime of fluorophores in different microenvironments. (a) TEM image of a catalyst particle consisting of a solid SiO_2 core decorated with Pt nanoparticles and then coated with a mesoporous SiO_2 shell. (b) Schematic showing the preferred orientation of Amplex red (blue platelets) and resorufin (red platelet) within the tunnel-like pores of the mesoporous SiO_2 shell. The white arrow indicates the dipole moment of a resorufin molecule. (c, d) Schematics showing the excitation of resorufin molecules (red squares) generated from the oxidation of Amplex red (black triangles) by Pt nanoparticles (gold spheres) on a SiO_2 core (dark gray sphere) within the pores (light gray cylinders) of the mesoporous SiO_2 shell. (c) Linearly polarized light will selectively excite resorufin molecules whose dipole moments align with the polarization direction (green arrows) of the incident laser excitation during SMF imaging. (d) Circularly polarized light (green spiral) will not lead to selective excitation. (e) Under linearly polarized light, an elliptical distribution of localizations was observed for resorufin molecules, indicating they are aligned within the tunnels of the mesoporous SiO_2 shell. (f) Under circularly polarized light, a circular distribution of localizations was observed. Panels (a) through (f) are adapted from ref 71 under a Creative Commons license.[223] (g) Schematic for the incorporation of a fluorescent BODIPY tag into either polynorbornene (R = H) or polydicyclopentadiene (R = polymer branches, cross-links, or the other half of the dicyclopentadiene monomer) through ring-opening metathesis polymerization using a third-generation ruthenium Grubbs catalyst. Approximately 1 in 10^7 monomer units incorporate the fluorescent label. (h) Fluorescence lifetime images during growth of polydicyclopentadiene particles before the Ru catalyst was added (left panel) and at different times after addition of the catalyst. The time after catalyst addition is given above each image. The molecular weight of the polymer determined by fluorescence lifetime imaging microscopy ($M_{W\ FLIM}$), and the intensity-averaged fluorescence lifetime (τ) are given below each image. The fluorescence lifetime increases as the polymer particles grow. Panels (g) and (h) are adapted with permission from ref 203. Copyright 2022 American Chemical Society.

tungsten oxide and bismuth oxybromide with low concentrations of crystal defects have band gaps between 2.8 and 2.9 eV and therefore do not absorb photons emitted by fluorescein or resorufin. However, in both tungsten oxide and bismuth oxybromide, the metal ions (i.e., W and Bi) can adopt different oxidation states. In such metal oxides and metal oxyhalides, the insertion of additional cations (e.g., H^+, Li^+, or Na^+) into the crystal lattice or the removal of oxygen anions (i.e., the creation of oxygen vacancies) leads to reduction of metal ions in the crystal for charge compensation (e.g., the reduction of W^{6+} to W^{5+} or W^{4+}. Note that both $W_{18}O_{49}$ and WO_3 are discussed in this article, which are different crystalline phases of tungsten oxide). These structural changes lead to sub-band gap absorption by the semiconductor at longer wavelengths. For example, Sambur and co-workers monitored the change in optical density of individual WO_3 nanorods during the electrochemical insertion of Li^+ ions and correlated the changes in transmission with the dynamics of ion insertion into different binding sites of the WO_3 lattice.[213]

Following this work, we correlated the photon counts of fluorescence bursts during SMF imaging of BiOBr nanoplates with the relative density of defects, including oxygen vacancies and Bi ions in a reduced oxidation state, in different nanoscale regions.[55] In the geometry for SMF imaging shown in Figure 2a, photons emitted from the activated probe must pass through the catalyst in order to be collected by the objective (this may not be the case in other geometries used for SMF imaging such as prism-based TIRF). We observed two populations among the BiOBr nanoplates using the coordinate-based colocalization algorithm described above for $W_{18}O_{49}$ nanowires.[55] The majority of BiOBr nanoplates exhibited a broad distribution of colocalization scores peaked near 0 for the photocatalytic oxidation of APF and reduction of resazurin, indicating the extraction of photogenerated holes and electrons were spatially uncorrelated. However, a subpopulation of particles contained a significantly greater number of spatially correlated events between the two probe reactions with colocalization scores greater than 0.9. The fluorescence bursts in colocalized regions of activity also exhibited higher photon counts relative to regions in which only oxidation or reduction occurred. The blue histograms in Figure 4f, g show photon counts from fluorescence bursts with colocalized activity (colocalization scores >0.9), while the red histograms show photon counts from bursts with uncorrelated activity (colocalization scores between −0.5 and

https://doi.org/10.1021/cbmi.3c00075
Chem. Biomed. Imaging 2023, 1, 692−715

0.5). These observations indicate that nanoscale regions with preferential activity for either oxidation or reduction (i.e., low colocalization scores) contain a higher concentration of midgap defect states that selectively trap photogenerated holes or electrons, respectively. Nanoscale regions of the BiOBr nanoplates containing a higher defect density will lead to greater absorption of photons emitted by the activated probe consistent with the lower photon counts for fluorescence bursts in these regions. Furthermore, regions with colocalized activity for both oxidation and reduction also displayed higher activity for the photocatalytic oxidation of APF, suggesting that the defects that lead to preferential activity for oxidation lower activity by mediating faster relaxation of photogenerated holes. The concentration and distribution of these defects vary both from particle to particle and across the surface of individual BiOBr nanoplates.

While the intensity burst is the primary indicator of a reaction event when using fluorogenic probes, the polarization and lifetime of emission from the activated probe can also be affected by its local environment.[71,203,204,214−218] For example, Fang and co-workers performed SMF imaging of the oxidation of Amplex red to resorufin using a nanoporous catalyst.[71] The catalyst consisted of a solid silica (SiO_2) core decorated with platinum nanoparticles and then coated with a mesoporous SiO_2 shell containing tunnel-like pores (with diameters between 2.2 and 3.3 nm) that radiate out from the center of the core (Figure 5a). To show that the motion of reactant and product molecules was restricted within the pores, they used linearly polarized light to excite the resorufin molecules generated within the pores of the catalyst. The elliptical distribution of localized fluorescence bursts under linearly polarized light (from multiple resorufin molecules) indicated that resorufin molecules were aligned within the tunnels of the mesoporous shell; this anisotropy is due to selective excitation of fluorophores that have their absorption dipole aligned with the polarization direction of the incident light (Figure 5b−f). Blum and co-workers designed a fluorescent BODIPY tag that is incorporated into polymer chains during the ring-opening metathesis polymerization (ROMP) of norbornene or dicyclopentadiene (Figure 5g).[203] They observed that the fluorescence lifetime of this tag increased as the polymer particles grew (Figure 5h), which indicated changes in the microenvironment of the fluorophore (possibly due to an increase in the local viscosity as the polymer chain length increased or, in the case of polydicyclopentadiene, as the number of cross-links in the polymer network increased).[204] While these examples were not done at the single-molecule level, advances in the ability to measure the three-dimensional orientation and fluorescence lifetime of single emitters[219,220] could provide new insights into how the confinement of solvent and substrate molecules in mesoporous catalysts (e.g., zeolites, metal organic frameworks, and layered transition metal chalcogenides) affects critical processes during heterogeneous catalysis including mass transport, solvation, and adsorption.[221,222]

The next fundamental question underlying the robustness of SMF microscopy is whether a catalyst with high activity for activating a fluorogenic probe will also exhibit high activity for other, more industrially relevant catalytic reactions. Performing ensemble catalytic measurements on the same samples used for single-molecule imaging is critical in determining the extent to which SMF imaging provides useful structure−activity trends. This type of correlation is not routine but is becoming more common in the SMF literature. In an early example, Chen and co-workers showed that the single-molecule activity of Au nanoparticles for activating fluorogenic probes was linearly correlated with their ensemble catalytic activity for similar reactions.[88] They studied two model reactions commonly used to evaluate the activity of metal nanoparticles at the ensemble level as they can be monitored by both absorption and Raman spectroscopy—the reduction of 4-nitrophenol and the oxidation of hydroquinone. They observed that larger spherical Au nanoparticles exhibited higher per-particle activities for both the reduction of resazurin at the single-molecule level (determined by counting the number of fluorescence bursts imaged per particle per second) and for the reduction of 4-nitrophenol to 4-aminophenol at the ensemble level. A similar correlation was observed for the oxidation of Amplex red at the single-molecule level and the oxidation of hydroquinone to 1,4-benzoquinone at the ensemble level.

Zhang and co-workers measured the photocatalytic activity of cadmium sulfide nanorods supported on graphitic carbon nitride (g-C_3N_4) nanosheets.[79] CdS/g-C_3N_4 heterostructures annealed at 300 °C exhibited higher activity for the photocatalytic reduction of protons to generate hydrogen at the ensemble level compared to samples prepared at room temperature. Through SMF imaging, they observed that resazurin was activated preferentially at the CdS nanorods for the sample annealed at 300 °C. On the other hand, this probe was activated at the edges of the g-C_3N_4 nanosheets for the sample prepared at room temperature. Thus, directing the flow of photogenerated electrons into the CdS nanorods made the CdS/g-C_3N_4 heterostructures more active for hydrogen evolution.

We propose that when a fluorogenic probe is activated by a chemical intermediate that is also produced during the reaction of interest, then the single-molecule activity should correlate well with the ensemble activity. For example, both Amplex red and APF can be activated into their fluorescence states by hydroxyl radicals, $^{\bullet}OH$. Hydroxyl radicals are a key intermediate during the oxidation of water to oxygen, which is the oxidative half of water splitting to generate hydrogen fuel.[81,224] As described above, when we used APF to image the photocatalytic generation of $^{\bullet}OH$ by $W_{18}O_{49}$ nanowires, we observed variations in activity along the lengths of the nanowires (Figure 6a, b).[81] The nanowires were synthesized via a hydrothermal method that did not use ligands that bind to their surface. We then used ascorbic acid as a ligand to functionalize the $W_{18}O_{49}$ nanowires and incorporate more oxygen vacancies through a photochemical process.[83] Under photoexcitation, the functionalized $W_{18}O_{49}$ nanowires extract electrons from surface-bound ascorbic acid molecules, which reduces tungsten ions and introduces additional oxygen vacancies for charge balance. Using SMF imaging, this photochemical process produced individual nanowires with higher and more uniform activity along their lengths compared to the initial nanowires (Figure 6c, d). Simultaneously, the ensemble production rate of oxygen during photocatalytic water oxidation nearly doubled after treating the nanowires with ascorbic acid. The combination of SMF imaging, surface characterization by X-ray photoelectron spectroscopy to identify changes in the average concentration of oxygen vacancies, and ensemble measurements of activity for photocatalytic water oxidation enabled us to conclude that the distribution of oxygen vacancies increased and became more uniform along the lengths of the nanowires after the photochemical treatment, which led to higher activity at both the single-molecule and ensemble levels.

https://doi.org/10.1021/cbmi.3c00075
Chem. Biomed. Imaging 2023, 1, 692−715

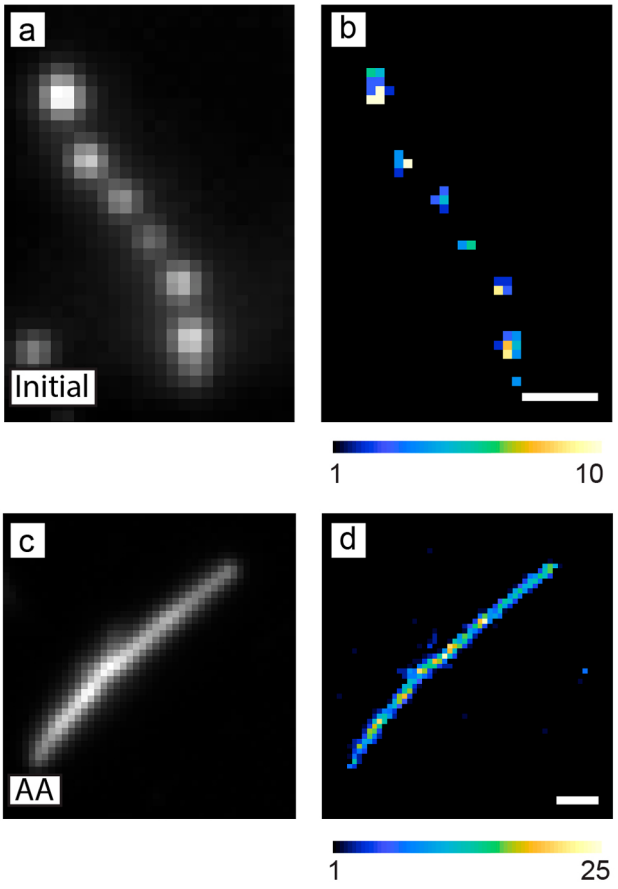

Figure 6. SMF microscopy using AFP to image photocatalytic •OH generation on individual $W_{18}O_{49}$ nanowires before and after surface functionalization. (a, c) Diffraction-limited fluorescence images prior to the localization of fluorescence bursts for (a) an as-synthesized nanowire and (c) a nanowire functionalized with ascorbic acid (AA). (b, d) Super-resolution activity maps of the same (b) as-synthesized nanowire and (d) ascorbic-acid-functionalized nanowire. The functionalized nanowire shows more uniform activity for this reaction along its length. Color scale: number of fluorescence bursts detected per 120 nm × 120 nm bin. Scale bars: 1 μm. Adapted with permission from ref 83. Copyright 2022 American Chemical Society.

In the above case of tungsten oxide, several pieces of evidence indicated that •OH radicals generated on the surface of the nanowires were the intermediate that activated APF.[81] DMSO, which is a scavenger for •OH radicals, quenched the activation of APF when it was added to the solution used for SMF imaging. At the ensemble level, the $W_{18}O_{49}$ nanowires could convert coumarin into 7-hydroxycoumarin, a reaction known to be mediated by •OH radicals.[225] Similarly, Sambur and Chen developed a kinetic model for the photoelectrochemical oxidation of Amplex red by individual TiO_2 nanorods that demonstrated the process was also mediated by •OH radicals.[224] While Amplex red was originally designed to detect H_2O_2 and APF to detect •OH radicals in biological samples,[207] it is important to note that both of these probes can also be directly oxidized by photogenerated holes in a photocatalyst. For example, our results indicate that BiOBr directly oxidizes APF using photogenerated holes rather than by generating •OH radicals.[55] For this photocatalyst, the reaction is not quenched by DMSO, and BiOBr is not active for the oxidation of coumarin to 7-hydroxycoumarin. Furthermore, there is the possibility that the fluorogenic probe can photosensitize the semiconductor photocatalyst. For example, TiO_2 nanocrystals can degrade Rhodamine B and other dye molecules using light that is absorbed by the dye molecule but not by TiO_2 (as the photon energy of the incident light is below the band gap of TiO_2).[226] In this case, the degradation of the dye occurs by photosensitization in which an electron transfers from the photoexcited dye molecule to the conduction band of TiO_2 (similar to a dye-sensitized solar cell) rather than by photocatalysis. As most commercially available fluorogenic probes also absorb visible light,[207] they could be photoexcited by the laser excitation used in SMF imaging and converted into their fluorescent form by transferring an electron to the semiconductor photocatalyst. Thus, to develop useful structure−activity trends through SMF imaging, it is critical to understand the chemical mechanism by which the fluorogenic probe is activated by the catalyst.

The above examples describe the challenges of using fluorogenic probes as proxies for catalytic activity and emerging techniques to extract additional information from these probes. The majority of fluorogenic probes we have described so far are commercially available (apart from the BODIPY derivatives shown in Figure 1b and Figure 5g, h). In the next section, we provide examples of new fluorogenic probes that could be applied to heterogeneous catalysis to image intermediates such as carbon monoxide, nitrite, and ammonia.

OPPORTUNITIES FOR USING NEW FLUOROGENIC PROBES TO IMAGE PHOTO- AND ELECTROCATALYSIS

We believe that the application of new fluorogenic probes in SMF imaging of nanoscale catalysts has significant potential to open new avenues for understanding the selectivity of these catalysts for generating specific chemical intermediates and/or selective bond activation. A variety of fluorogenic probes have been developed in the context of imaging small molecules, such as nitric oxide, carbon monoxide, hydrogen sulfide, nitrite, and reactive oxygen species that act as chemical signaling agents and/or toxins in the human body.[227−229] Fluorogenic probes have also been developed for detecting contaminants in drinking water and food.[230] These probes could be applied to SMF microscopy of electro- and photocatalysts for fuel production and environmental remediation to image reaction events in situ and develop structure−activity relationships for these catalysts. Here, we give representative examples of chemically activated fluorogenic probes for detecting CO, NO_2^-, and NH_3. There are review articles that discuss a wider range of molecular probes for detecting these species and other small molecules.[207,227−230]

Electrocatalysts and photocatalysts that can reduce carbon dioxide into formic acid, methanol, ethanol, propanol, ethylene, and other products containing C−C bonds could provide a way to remove this greenhouse gas from the atmosphere and convert it into useful chemical feedstocks.[10−14] Carbon monoxide can be either an intermediate or the product in electro/photocatalytic CO_2 reduction. In the case where CO is the end product, other catalysts can be used to further reduce it to the feedstocks above.[235] The probes shown in Figure 7a, b were developed for detecting CO in live cells due to its toxicity to animals and the role it plays (in small quantities) in the body as a neurotransmitter. For the probe COP-1 shown in Figure 7a, the bound palladium initially quenches the fluorescence of the BODIPY derivative.[202] Binding CO releases Pd(0), which activates the probe into its fluorescent state. The fluorescence quantum yield of COP-1 increases from 1% to 44% after activation. COP-1 can

https://doi.org/10.1021/cbmi.3c00075
Chem. Biomed. Imaging 2023, 1, 692−715

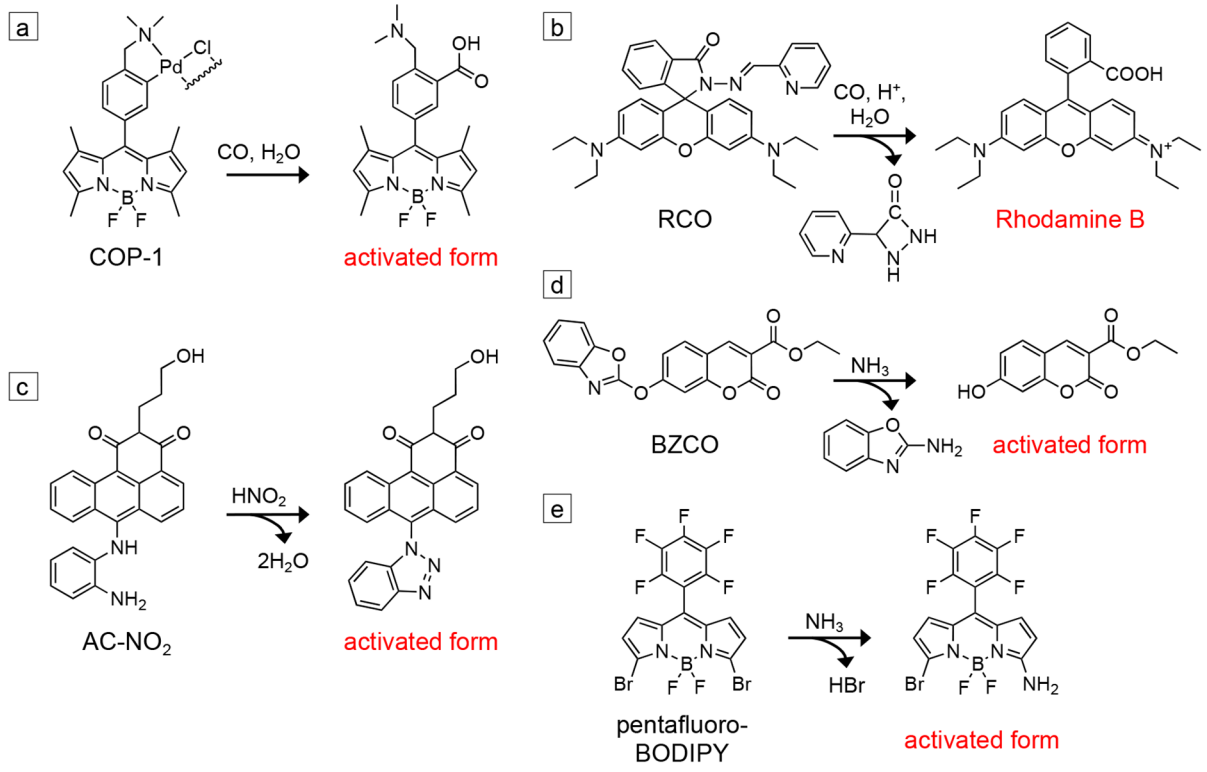

Figure 7. Potential fluorogenic probes for detecting reaction intermediates and products during SMF imaging of nanoscale catalysts. (a) COP-1 reacts with carbon monoxide to generate a fluorescent BODIPY derivative.[202] (b) RCO reacts with CO and protons to produce Rhodamine B.[231] (c) AC-NO_2 reacts with nitrite to form a fluorescent anthracene derivative.[232] (d) BZCO reacts with ammonia and other amines to form a fluorescent 7-hydroxycoumarin derivative.[233] (e) Pentafluoro-BODIPY reacts with NH_3 vapor to form a fluorescent BODIPY derivative.[234]

detect micromolar concentrations of CO and is highly selective for being activated by CO relative to other potential analytes present in living cells (e.g., H_2O_2, NaOCl, $^{\bullet}O_2^-$, NO, and H_2S). Similarly, the RCO fluorogenic probe shown in Figure 7b was synthesized using Rhodamine B as the starting material.[231] It is activated in the presence of CO and protons to reform Rhodamine B. RCO can detect CO in nanomolar concentrations, exhibits high selectivity for CO, and unlike many probes developed for CO detection, does not require Pd for activation.

In the cases of both COP-1 and RCO, the ruthenium complex [$Ru(CO)_3Cl$(glycinate)] was used as the CO source to titrate the increase in fluorescence intensity of the probe with known concentrations of CO. Testing the activation of these probes by electro/photocatalysts that generate CO would first be necessary, using fluorescence spectroscopy at the ensemble level, before determining if their activated forms can be detected at the single-molecule level. The pH dependence of these CO probes would also need to be tested. Both COP-1 and RCO were tested in aqueous phosphate buffer with pH 7.4 (i.e., the buffer solution typically used for fluorescence imaging of live cells). The quantum yield of the RCO probe did not change significantly over a pH range of 6.0 to 8.5. However, solutions saturated with CO_2 are often used for testing electro- and photocatalysts for CO_2 reduction, which will have a pH near 3.9. Furthermore, these probes were used in micromolar concentrations to detect CO, whereas nanomolar concentrations of fluorogenic probes are often used for SMF imaging. Finally, while the selectivity of COP-1, RCO, and similar probes for CO are often tested in the presence of species that could interfere with their activation in living cells (e.g., H_2O_2, $^{\bullet}O_2^-$, NO, NO_2^-, H_2S),[202,229,231,236] the potential for activation by other intermediates and products generated during electro/photocatalytic CO_2 reduction would need to be evaluated. For example, the hydrogen evolution reaction (i.e., the reduction of protons or water to H_2) is a competing process during CO_2 reduction as it occurs at a similar thermodynamic potential. To test for activation by H_2, SMF imaging with the probe could be performed first in an aqueous solution with CO_2 excluded. The possibility for products of further reduction of CO, such as formate, to activate these probes would also need to be determined. If these probes are indeed selective for CO over other potential products, a useful comparison would be to image the same catalyst sample with both resazurin and the CO-selective fluorogenic probe. The colocalization analysis described above could be used to evaluate whether the same sites that activate resazurin through direct electro/photocatalytic reduction are also responsible for generating CO.

Electrocatalysts and photocatalysts are also being developed for environmental remediation. For example, nitrate, NO_3^-, is found in water sources as a byproduct of fertilizers used in agriculture and from industrial runoff. As high concentrations of NO_3^- in drinking water are harmful, catalysts are needed to reduce NO_3^- to nitrogen, N_2, and/or ammonia, NH_3.[19−21] Simultaneously, fluorogenic probes have been developed to detect nitrite, NO_2^-, a common additive in meat products, as NO_2^- can degrade to produce carcinogenic compounds.[230,232,237] As NO_2^- is an intermediate in the reduction of NO_3^-, these fluorogenic probes could be employed in SMF imaging of electro/photocatalysts for NO_3^- reduction. For example, the probe AC-NO_2 shown in Figure 7c is an anthracene carboxyimide derivative designed for the detection of NO_2^-.[232] Emission from the probe is initially quenched due to

https://doi.org/10.1021/cbmi.3c00075
Chem. Biomed. Imaging 2023, 1, 692−715

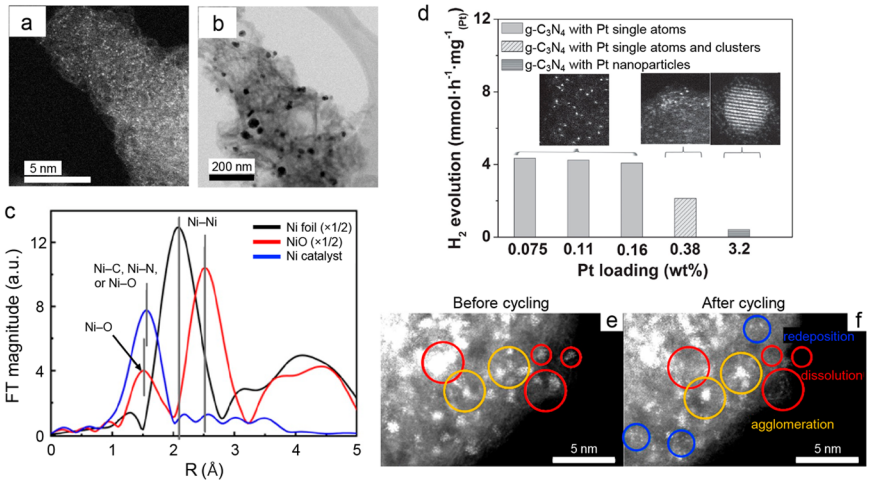

Figure 8. Characterization of SACs. (a) STEM image of dispersed Ni atoms and (b) TEM image of Ni nanoparticles supported on g-C_3N_4 in different regions of the same sample. (c) FT-EXAFS spectra of a metallic nickel foil (black trace), nickel oxide (red trace) and the Ni/g-C_3N_4 catalyst sample shown in panels (a) and (b). The first peak in the Ni foil corresponds to the average Ni−Ni distance. The first peak in the NiO sample corresponds to the Ni−O distance, while the second peak corresponds to the Ni−Ni distance. The first peak in the Ni/g-C_3N_4 sample corresponds to Ni−C and Ni−N distances. Panels (a) through (c) are adapted from ref 263, with the permission of AIP publishing. (d) Comparison of photocatalytic activity for hydrogen evolution using different samples of Pt on g-C_3N_4 normalized per Pt atom. The insets show STEM images of representative samples containing either single Pt atoms, a mixture of single Pt atoms and clusters, or Pt nanoparticles as the loading of Pt on the g-C_3N_4 support increases. Panel (d) is adapted with permission from ref 251. Copyright John Wiley and Sons 2016. (e, f) STEM imaging of the same region of a Pt SAC on a carbon support (e) before and (f) after electrochemical cycling between 0.6 and 1.5 V vs the reversible hydrogen electrode in 0.1 M $HClO_4$ for 1000 cycles. Panels (e) and (f) are adapted with permission from ref 262. Further permissions related to panels (e) and (f) should be directed to ACS.

photoinduced electron transfer (PET) from the aryl diamine. When this group reacts with NO_2^- to form a triazole, PET is quenched, and the probe becomes fluorescent. The fluorescence quantum yield of AC-NO_2 increases from 0.3% to 42% after activation. The probe has a detection limit of 84 nM for NO_2^- and good selectivity for activation by NO_2^- relative to reactive oxygen species such as H_2O_2 and ClO^-. The probe was tested in aqueous solutions containing ethanol and hydrochloric acid, and its response exhibits a strong pH dependence. The increase in fluorescence intensity upon exposure to NO_2^- is greatest at pH 1, but the response drops with increasing pH until there is no fluorescence enhancement at pH 5.

In addition to catalysts that can degrade the byproducts of fertilizers such as nitrate, electro- and photocatalysts are also needed to convert nitrogen gas into ammonia (i.e., the primary component of fertilizers). The Haber−Bosch process combines H_2 from natural gas and N_2 to make NH_3 at elevated temperatures and pressures. Developing low-temperature methods to produce NH_3 using renewable energy sources would significantly reduce the energy consumption and carbon emissions that result from the Haber−Bosch process.[11,15−18] Similar to CO and NO_2^-, fluorogenic probes have been developed to detect NH_3 and other amines in water sources and food.[230,233,234,238] For example, in the BZCO probe shown in Figure 7d, the benzoxazole group inhibits internal charge transfer in the molecule, which initially leads to a low fluorescence quantum yield. Cleavage of the benzoxazole group by an amine produces a fluorescent 7-hydroxycoumarin derivative.[233] The probe is soluble in common organic solvents including acetonitrile, dichloromethane, DMSO, ethyl acetate, and toluene. In addition to NH_3, BZCO can be activated by a variety of primary and secondary amines, such as propylamine, dimethylamine, diethylamine, and cyclohexylamine. This lack of selectivity may be undesirable in cases where the nanoscale catalyst is passivated with alkyl amine ligands as the ligands may also activate this probe. When the BZCO dye was evaporated onto filter paper to make a paper-based sensor, the detection limit for propylamine vapor was 3.8 ppm. While BZCO can be activated by NH_3 as well as various alkylamines, the pentafluoro-BODIPY probe shown in Figure 7e was found to be selective for NH_3 relative to other amines.[234] Nucleophilic substitution of one of the bromines by NH_3 leads to activation of the probe. The detection limit was between 15 and 18 parts per billion for NH_3 vapor. The probe is compatible with a variety of polar organic solvents, including acetonitrile, DMSO, methanol, and tetrahydrofuran. However, the contrast between the initial and activated states is lower for this probe relative to the other fluorogenic probes discussed in both Figure 1 and Figure 7. The quantum yield is 45% in the initial form and then increases to 61% after exposure to NH_3. Further modifications of the substituents around such BODIPY dyes may increase the fluorescence contrast for the detection of NH_3.

In cases where the source of nitrogen for NH_3 production could potentially come from residual nitrogen-containing species on the surface of the catalyst or from the degradation of a nitrogen-containing catalyst (e.g., g-C_3N_4),[239,240] in situ imaging by SMF microscopy during the generation of NH_3 using probes such as those shown in Figure 7d, e would be valuable to monitor changes in the activity of different nanoscale regions. Decreases in activity over time would indicate the nitrogen came from adventitious surface species or from catalyst degradation. For catalysts that can reduce NO_3^- all the way to NH_3, probes such as those shown in Figure 7c, d could be used in sequence to compare the regions of the catalyst that are active for generating NO_2^- vs NH_3.

https://doi.org/10.1021/cbmi.3c00075
Chem. Biomed. Imaging 2023, 1, 692−715

OPPORTUNITIES TO IMAGE NOVEL CATALYSTS WITH SINGLE-MOLECULE FLUORESCENCE MICROSCOPY

Based on the challenges and opportunities in SMF imaging discussed above, we provide an example of a nanoscale catalytic system that is, so far, underexplored in SMF imaging and describe how this technique could provide new insights into these materials. We believe that SMF imaging has significant potential to understand heterogeneity in the catalytic activity of single-atom catalysts. The deposition of metal and metal oxide nanoparticles, such as Pt, Ni, Ag, Au, and IrO_2 onto semiconductor photocatalysts is a common strategy to enhance charge separation and provide reaction sites that lower the kinetic barrier for the reaction of interest (e.g., water oxidation or CO_2 reduction).[241−246] SMF imaging of Au nanoparticles deposited on TiO_2[74] and CdS[75] photocatalysts has shown that fluorogenic probes are selectively activated at the nanoparticle catalysts deposited on these semiconductors. On the other hand, single-atom catalysts (SACs) are typically composed of individually dispersed metal atoms stabilized on a support such as graphene, g-C_3N_4, or a metal oxide. They offer several advantages over nanoparticle catalysts, including more efficient use of expensive metals (as in principle every metal atom is exposed at the surface and serves as a reaction site) and the ability to tune the ligand field of the metal centers based on how the metal atoms are coordinated to the support in a manner analogous to homogeneous coordination complexes.[1,247−250] SACs have been reported to be more active and stable relative to nanoparticles composed of the same metal for a variety of photocatalytic and electrocatalytic reactions, including hydrogen evolution,[251−254] CO_2 reduction,[255−259] and the reduction of nitrogen to ammonia.[260,261] For example, Figure 8d shows the activity for photocatalytic hydrogen evolution normalized per Pt atom in which SACs of Pt dispersed on g-C_3N_4 show higher activity than Pt nanoparticles.[251]

SACs have been primarily characterized using ex-situ techniques, with a focus on their atomic-level structure: aberration-corrected STEM, X-ray diffraction (XRD), X-ray photoelectron spectroscopy (XPS), and X-ray absorption spectroscopy (XAS) are widely used to evidence the single-atom nature of SACs. While these techniques yield useful structural information, it is important to recognize their inherent limitations. HAADF-STEM imaging can identify dispersed metal atoms based on contrast introduced by differences in atomic number (i.e., Z contrast). In many SACs, the metal atoms have a higher atomic number than the support (Figure 8a).[251,253,254,256−260,262] This technique can also differentiate between single atoms and clusters or nanoparticles based on mass contrast. However, STEM imaging is typically only performed on small regions of the catalyst ($\leq 25 \times 25$ nm^2). Thus, the area imaged may not always be representative of the entire sample. XRD has been used to indicate the lack of crystalline metal nanoparticles (suggesting the presence of dispersed atoms),[251,253,256,259−261] but is insensitive to small quantities of nanoparticles. XPS provides information on the oxidation state of the metal atoms in the SAC,[254,256−259,261,262] which can potentially rule out metal−metal bonding, but XPS averages over the heterogeneous coordination environments of the metal atoms and/or clusters. The extended X-ray absorption fine structure (EXAFS) from XAS is the primary technique that is used to rule out metal−metal bonding and provide evidence against the formation of clusters or nanoparticles.[251−254,256−261] The first peak in a Fourier-transformed (FT) EXAFS spectrum indicates the first coordination shell, while the second peak indicates the second coordination shell. The idea is that the second peak should be missing for dispersed metals that are truly single atoms but will be present in metal clusters and nanoparticles. However, like XPS, EXAFS also averages over the different coordination environments of metal atoms in the sample. The second peak (i.e., the marker of clusters and nanoparticles) may not be observable when the sample contains a mixture of single atoms and clusters. For example, Feng et al. showed that a sample containing both individually dispersed Ni atoms (Figure 8a) and Ni nanoparticles (Figure 8b) on a g-C_3N_4 support lacked the second peak in its FT-EXAFS spectrum (Figure 8c) and thus could be interpreted as only possessing individually dispersed Ni atoms.[263] In this sample and others like it, the relative contributions of single atoms, clusters, and nanoparticles to the observed catalytic activity would be averaged over using ensemble measurements. Recent studies have shown that clusters and nanoparticles can form when SACs are in their catalytically active state and contribute significantly to the observed activity.[58] Thus, several questions regarding structure−activity relationships in SACs remain unanswered. How do different coordination geometries for binding the dispersed metal atoms on the support and their proximity to other active sites affect the local activity? What are the relationships between the activity of single metal atoms and the microenvironment of the support (e.g., from local strain in two-dimensional supports like graphene and g-C_3N_4 or from defects in the support)? Are the active sites stable over time or do their activities fluctuate (e.g., due to agglomeration of the atoms or changes in their interaction with the support)?

In an initial application of SMF microscopy of SACs, Xu and co-workers studied single Pt atoms on ceria (CeO_2) nanocrystals for the reduction of resazurin using H_2 as a reductant.[99] They observed higher activity per Pt atom for the Pt/CeO_2 SAC compared with Pt nanoparticles. Through analyzing the dependence of the average on and off times of fluorescence bursts on the concentrations of resazurin and H_2 combined with calculations using density functional theory, they proposed that both resazurin and resorufin bind more strongly to Pt atoms of the SAC compared to Pt nanoparticles. Furthermore, individual Pt atoms interact more strongly with the CeO_2 support relative to surface Pt atoms on a Pt nanoparticle, which could inhibit catalysis-induced restructuring for the SAC. However, in this study, each CeO_2 nanocrystal contained on average only one Pt atom. Thus, agglomeration of Pt atoms into clusters would not be observed. So far, SMF imaging has not been used to create super-resolution activity maps of SACs.

The role of single-atom sites in enhancing photocatalytic activity has many parallels to the role of oxygen vacancies in metal oxide semiconductors. Experimental and theoretical studies have shown that both oxygen vacancies and SACs can enhance activity by increasing light absorption,[33,35,37,82] increasing charge separation between photoexcited electrons and holes,[33,35,36,251−254,260] and/or acting as preferential adsorption sites for reactant molecules.[35−37,255,260] However, these studies typically treat the active sites individually and have not yet looked at interactions and cooperativity between neighboring sites. Based on the work described above for SMF imaging of tungsten oxide nanowires containing oxygen vacancies, we expect that SACs will show similar nanoscale variations in which their activity is concentrated in "hot spots" across the catalyst surface. These variations could arise from

https://doi.org/10.1021/cbmi.3c00075
Chem. Biomed. Imaging 2023, 1, 692−715

differences in the local concentration of the dispersed metal atoms, their coordination to the support, or the presence of clusters or nanoparticles in specific regions of the catalyst. Conclusive identification of the structure of individual catalytic hot spots in SACs imaged by SMF microscopy would require correlative imaging with HAADF-STEM. However, with SMF microscopy alone, analysis of the fluorescence bursts would provide evidence on whether the active regions contain single atoms or nanoparticles. As described above, Xu and co-workers observed different dependencies for $\langle\tau_{off}\rangle^{-1}$ and $\langle\tau_{on}\rangle^{-1}$ of fluorescence bursts for single Pt atoms supported on CeO_2 and Pt nanoparticles.[99] Thus, for particles containing both of these types of active sites, they could be distinguished by fitting their concentration dependence to a Langmuir−Hinshelwood model. While correlative imaging between SMF and either STXM or TERS has not yet been reported, their spatial resolutions are comparable. Combining SMF imaging with either of these techniques would be a powerful way to connect differences in nanoscale activity with chemical information on the coordination environment of the metal atoms on the support.

The new fluorogenic probes described in the previous section would be advantageous for studying single-atom catalysts that are being developed for reduction of CO_2 to CO and the reduction of N_2 to NH_3.[255−261] Using a probe activated by CO such as COP-1 or RCO (Figure 7a, b) in correlation with a typical probe for reduction reactions such as resazurin could clarify the catalytic mechanism of CO_2 reduction on the SAC. For instance, colocalization of activity maps for the activation of resazurin and COP-1 could determine whether the sites where the extraction of photoexcited electrons occurs are also preferential sites for the reduction of CO_2. Since many SACs are being developed for these industrially relevant reactions, the new probes would enable SMF imaging to be applied to these reactions directly, rather than using proxy reactions.

Evidence that SACs remain stable as dispersed single atoms after catalysis is typically done by ex situ EXAFS and STEM. Due to the limitation of these techniques discussed above, SMF imaging could be used as an in situ technique to map local changes in the catalytic activity of SACs due to restructuring when they are in their active state. For example, Speck et al., used ex situ STEM to image the same region of a Pt SAC before and after electrochemical cycling (Figure 8e, f).[262] They observed dissolution of Pt atoms, the redeposition of Pt in regions of the carbon support that did not initially contain it, and agglomeration of the single atoms to form clusters. SMF imaging is well suited to observe how the different time scales of these processes affect activity. Changes in the spatial distribution of active regions over time would indicate reorganization of the active sites. Dissolution of dispersed metal atoms in the SAC would lead to a decrease in the activity of a specific nanoscale region, while their redeposition in a new area would lead to an increase. Agglomeration of metal atoms could lead to either an increase or decrease in activity. Analysis of the on and off times of fluorescence bursts could help to distinguish these processes. The power of SMF microscopy in this case relative to other imaging techniques described at the beginning of this article would be to monitor in real time changes in activity of different nanoscale regions during catalytic turnovers and potential restructuring and/or degradation that occur during catalysis.

CONCLUSIONS

Beyond just localizing fluorescence intensity bursts during SMF microscopy of nanoscale catalysts, correlation with other microscopies or between multiple fluorogenic probes is critical to connect the observed variations in activity with structural, chemical, and/or morphological features of the catalyst. Quantifying the orientation and fluorescence lifetime of fluorophores within porous catalysts can provide information on their local environment. In the future, correlation with other microscopies, such as Kelvin probe force microscopy (KPFM) and TERS, will be beneficial in developing structure−activity relationships in nanoscale catalysts. KPFM could be used to image the local electric surface potential across semiconductor photocatalysts.[264,265] TERS could measure changes in the coverage of ligand-passivated nanoparticles in situ during catalysis.[266,267] To ensure that fluorogenic probes provide valuable structure−activity trends, it is important to measure both the single-molecule/single-particle activity and the ensemble activity for the same sample, and when possible, to use fluorogenic probes that are activated through similar chemical mechanisms as industrially relevant catalytic reactions. The application of fluorogenic probes that can detect CO, NO_2^-, NH_3, and other intermediates will help in monitoring the selectivity of nanoscale electro- and photocatalysts for generating the desired products during fuel production and environmental remediation. Together, novel fluorogenic probes and correlative imaging can expand SMF imaging to a wider range of nanoscale catalysts such as single-atom catalysts and semiconductors with surface-attached molecular catalysts.[268−270] As SMF imaging of nanoscale catalysts is primarily done in aqueous solution, there is also the need to expand this technique to new chemical environments, such as nanoparticle catalysts and inorganic coordination complexes embedded in polymer matrices for photo- and electrocatalytic fuel production.[25−27,271−273]

AUTHOR INFORMATION

Corresponding Author

Bryce Sadtler − *Department of Chemistry, Washington University, St. Louis, Missouri 63130, United States; Institute of Materials Science & Engineering, Washington University, St. Louis, Missouri 63130, United States;* orcid.org/0000-0003-4860-501X; Email: sadtler@wustl.edu

Authors

Meikun Shen − *Department of Chemistry and Biochemistry, University of Oregon, Eugene, Oregon 97403, United States;* orcid.org/0000-0001-8100-4115

William H. Rackers − *Department of Chemistry, Washington University, St. Louis, Missouri 63130, United States;* orcid.org/0000-0002-1658-2389

Complete contact information is available at: https://pubs.acs.org/10.1021/cbmi.3c00075

Notes

The authors declare no competing financial interest.

ACKNOWLEDGMENTS

This material is based upon work supported by the National Science Foundation (NSF) under grant no. CHE-1753344 to B.S. The Authors thank J. S. Bates for useful discussions regarding SACs and EXAFS.

VOCABULARY

Fluorogenic probe, A molecule that is initially nonfluorescent or weakly fluorescent but becomes highly fluorescent after undergoing a chemical or physical change; Total internal reflection fluorescence (TIRF) microscopy, A form of fluorescence microscopy in which the incident angle for laser excitation is such that the illumination is totally internally reflected between the top and bottom surfaces of a microscope coverslip. An evanescent field is created that only excites fluorescent molecules near the surface of the coverslip; Superlocalization, Fitting the emission profile or point spread function of a single fluorophore to localize its position below the diffraction-limited resolution of an optical microscope; Correlative imaging, Imaging the same region of a sample using two different microscopy techniques, such as single-molecule fluorescence microscopy and electron microscopy and correlating information gained from each technique; Nanoscale catalyst, Catalyst particles in which at least one dimension is in the range of 1 to 100 nm. Nanoscale catalysts can be composed of metals, metal oxides, metal chalcogenides as well as combinations of these materials and include spherical nanoparticles, nanorods, nanowires, and nanoplates; Single-atom catalyst, A catalyst in which the active sites consist of individually dispersed atoms (typically metal atoms but can also be nonmetals) that are bound to the surface of a support.[1] The support could be another metal, metal oxide, or a conductive form of carbon. The type of support and how the dispersed atoms are coordinated to it strongly influence the electronic structure activity, and stability of the active sites

REFERENCES

(1) Kaiser, S. K.; Chen, Z.; Faust Akl, D.; Mitchell, S.; Pérez-Ramírez, J. Single-Atom Catalysts across the Periodic Table. *Chem. Rev.* **2020**, *120*, 11703−11809.

(2) Weiss, E. A. Designing the Surfaces of Semiconductor Quantum Dots for Colloidal Photocatalysis. *ACS Energy Letters* **2017**, *2*, 1005−1013.

(3) Li, X.-B.; Xin, Z.-K.; Xia, S.-G.; Gao, X.-Y.; Tung, C.-H.; Wu, L.-Z. Semiconductor Nanocrystals for Small Molecule Activation Via Artificial Photosynthesis. *Chem. Soc. Rev.* **2020**, *49*, 9028−9056.

(4) Yu, Y.; Ma, T.; Huang, H. Semiconducting Quantum Dots for Energy Conversion and Storage. *Adv. Funct. Mater.* **2023**, *33*, 2213770.

(5) Huang, H.; Jiang, L.; Yang, J.; Zhou, S.; Yuan, X.; Liang, J.; Wang, H.; Wang, H.; Bu, Y.; Li, H. Synthesis and Modification of Ultrathin g-C_3N_4 for Photocatalytic Energy and Environmental Applications. *Renewable and Sustainable Energy Reviews* **2023**, *173*, 113110.

(6) Hou, Y.; Zhuang, X.; Feng, X. Recent Advances in Earth-Abundant Heterogeneous Electrocatalysts for Photoelectrochemical Water Splitting. *Small Methods* **2017**, *1*, 1700090.

(7) Opoku, F.; Govender, K. K.; van Sittert, C. G. C. E.; Govender, P. P. Recent Progress in the Development of Semiconductor-Based Photocatalyst Materials for Applications in Photocatalytic Water Splitting and Degradation of Pollutants. *Advanced Sustainable Systems* **2017**, *1*, 1700006.

(8) Chen, S.; Huang, D.; Xu, P.; Xue, W.; Lei, L.; Cheng, M.; Wang, R.; Liu, X.; Deng, R. Semiconductor-Based Photocatalysts for Photocatalytic and Photoelectrochemical Water Splitting: Will We Stop with Photocorrosion? *Journal of Materials Chemistry A* **2020**, *8*, 2286−2322.

(9) Takata, T.; Jiang, J.; Sakata, Y.; Nakabayashi, M.; Shibata, N.; Nandal, V.; Seki, K.; Hisatomi, T.; Domen, K. Photocatalytic Water Splitting with a Quantum Efficiency of Almost Unity. *Nature* **2020**, *581*, 411−414.

(10) Low, J.; Yu, J.; Ho, W. Graphene-Based Photocatalysts for CO_2 Reduction to Solar Fuel. *J. Phys. Chem. Lett.* **2015**, *6*, 4244−4251.

(11) Yang, J.; Guo, Y.; Lu, W.; Jiang, R.; Wang, J. Emerging Applications of Plasmons in Driving CO_2 Reduction and N_2 Fixation. *Adv. Mater.* **2018**, *30*, 1802227.

(12) Gao, D.; Zhou, H.; Cai, F.; Wang, J.; Wang, G.; Bao, X. Pd-Containing Nanostructures for Electrochemical CO_2 Reduction Reaction. *ACS Catal.* **2018**, *8*, 1510−1519.

(13) Kim, C.; Dionigi, F.; Beermann, V.; Wang, X.; Möller, T.; Strasser, P. Alloy Nanocatalysts for the Electrochemical Oxygen Reduction (ORR) and the Direct Electrochemical Carbon Dioxide Reduction Reaction (CO_2RR). *Adv. Mater.* **2019**, *31*, 1805617.

(14) Shyamal, S.; Pradhan, N. Halide Perovskite Nanocrystal Photocatalysts for CO_2 Reduction: Successes and Challenges. *J. Phys. Chem. Lett.* **2020**, *11*, 6921−6934.

(15) Shi, R.; Zhao, Y.; Waterhouse, G. I. N.; Zhang, S.; Zhang, T. Defect Engineering in Photocatalytic Nitrogen Fixation. *ACS Catal.* **2019**, *9*, 9739−9750.

(16) Shen, H.; Yang, M.; Hao, L.; Wang, J.; Strunk, J.; Sun, Z. Photocatalytic Nitrogen Reduction to Ammonia: Insights into the Role of Defect Engineering in Photocatalysts. *Nano Research* **2022**, *15*, 2773−2809.

(17) Qing, G.; Ghazfar, R.; Jackowski, S. T.; Habibzadeh, F.; Ashtiani, M. M.; Chen, C.-P.; Smith, M. R., III; Hamann, T. W. Recent Advances and Challenges of Electrocatalytic N_2 Reduction to Ammonia. *Chem. Rev.* **2020**, *120*, 5437−5516.

(18) Zhang, G.; Sewell, C. D.; Zhang, P.; Mi, H.; Lin, Z. Nanostructured Photocatalysts for Nitrogen Fixation. *Nano Energy* **2020**, *71*, 104645.

(19) Roy, S. Photocatalytic Materials for Reduction of Nitroarenes and Nitrates. *J. Phys. Chem. C* **2020**, *124*, 28345−28358.

(20) Xu, H.; Ma, Y.; Chen, J.; Zhang, W.-x.; Yang, J. Electrocatalytic Reduction of Nitrate - a Step Towards a Sustainable Nitrogen Cycle. *Chem. Soc. Rev.* **2022**, *51*, 2710−2758.

(21) Liang, X.; Zhu, H.; Yang, X.; Xue, S.; Liang, Z.; Ren, X.; Liu, A.; Wu, G. Recent Advances in Designing Efficient Electrocatalysts for Electrochemical Nitrate Reduction to Ammonia. *Small Structures* **2023**, *4*, 2200202.

(22) Akhundi, A.; Badiei, A.; Ziarani, G. M.; Habibi-Yangjeh, A.; Muñoz-Batista, M. J.; Luque, R. Graphitic Carbon Nitride-Based Photocatalysts: Toward Efficient Organic Transformation for Value-Added Chemicals Production. *Molecular Catalysis* **2020**, *488*, 110902.

(23) Li, J.-Y.; Li, Y.-H.; Qi, M.-Y.; Lin, Q.; Tang, Z.-R.; Xu, Y.-J. Selective Organic Transformations over Cadmium Sulfide-Based Photocatalysts. *ACS Catal.* **2020**, *10*, 6262−6280.

(24) Yuan, Y.; Jin, N.; Saghy, P.; Dube, L.; Zhu, H.; Chen, O. Quantum Dot Photocatalysts for Organic Transformations. *J. Phys. Chem. Lett.* **2021**, *12*, 7180−7193.

(25) Wang, Y.-J.; Long, W.; Wang, L.; Yuan, R.; Ignaszak, A.; Fang, B.; Wilkinson, D. P. Unlocking the Door to Highly Active ORR Catalysts for PEMFC Applications: Polyhedron-Engineered Pt-Based Nanocrystals. *Energy Environ. Sci.* **2018**, *11*, 258−275.

(26) Zhao, Z.; Chen, C.; Liu, Z.; Huang, J.; Wu, M.; Liu, H.; Li, Y.; Huang, Y. Pt-Based Nanocrystal for Electrocatalytic Oxygen Reduction. *Adv. Mater.* **2019**, *31*, 1808115.

(27) Su, Y.-W.; Lin, W.-H.; Hsu, Y.-J.; Wei, K.-H. Conjugated Polymer/Nanocrystal Nanocomposites for Renewable Energy Applications in Photovoltaics and Photocatalysis. *Small* **2014**, *10*, 4427−4442.

(28) Jaramillo, T. F.; Jorgensen, K. P.; Bonde, J.; Nielsen, J. H.; Horch, S.; Chorkendorff, I. Identification of the Active Edge Sites for Electrochemical H_2 Evolution from MoS_2 Nanocatalysts. *Science* **2007**, *317*, 100−102.

(29) Kibsgaard, J.; Chen, Z.; Reinecke, B. N.; Jaramillo, T. F. Engineering the Surface Structure of MoS_2 To preferentially Expose Active Edge Sites For Electrocatalysis. *Nat. Mater.* **2012**, *11*, 963−969.

(30) Balasubramanyam, S.; Shirazi, M.; Bloodgood, M. A.; Wu, L.; Verheijen, M. A.; Vandalon, V.; Kessels, W. M. M.; Hofmann, J. P.; Bol, A. A. Edge-Site Nanoengineering of WS_2 by Low-Temperature Plasma-Enhanced Atomic Layer Deposition for Electrocatalytic Hydrogen Evolution. *Chem. Mater.* **2019**, *31*, 5104−5115.

https://doi.org/10.1021/cbmi.3c00075
Chem. Biomed. Imaging 2023, 1, 692−715

(31) Kauffman, D. R.; Deng, X.; Sorescu, D. C.; Nguyen-Phan, T.-D.; Wang, C.; Marin, C. M.; Stavitski, E.; Waluyo, I.; Hunt, A. Edge-Enhanced Oxygen Evolution Reactivity at Ultrathin, Au-Supported Fe_2O_3 Electrocatalysts. *ACS Catal.* **2019**, *9*, 5375−5382.
(32) Kashale, A. A.; Ghule, A. V.; Chen, I.-W. P. Active Edge Site Exposed β-$Ni(OH)_2$ Nanosheets on Stainless Steel Mesh as a Versatile Electrocatalyst for the Oxidation of Urea, Hydrazine, and Water. *ChemCatChem.* **2021**, *13*, 1165−1174.
(33) Chen, X.; Liu, L.; Yu, P. Y.; Mao, S. S. Increasing Solar Absorption for Photocatalysis with Black Hydrogenated Titanium Dioxide Nanocrystals. *Science* **2011**, *331*, 746−750.
(34) Wang, J.; Wang, Z.; Huang, B.; Ma, Y.; Liu, Y.; Qin, X.; Zhang, X.; Dai, Y. Oxygen Vacancy Induced Band-Gap Narrowing and Enhanced Visible Light Photocatalytic Activity of ZnO. *ACS Appl. Mater. Interfaces* **2012**, *4*, 4024−4030.
(35) Guan, M.; Xiao, C.; Zhang, J.; Fan, S.; An, R.; Cheng, Q.; Xie, J.; Zhou, M.; Ye, B.; Xie, Y. Vacancy Associates Promoting Solar-Driven Photocatalytic Activity of Ultrathin Bismuth Oxychloride Nanosheets. *J. Am. Chem. Soc.* **2013**, *135*, 10411−10417.
(36) Khan, M. M.; Ansari, S. A.; Pradhan, D.; Ansari, M. O.; Han, D. H.; Lee, J.; Cho, M. H. Band Gap Engineered TiO_2 Nanoparticles for Visible Light Induced Photoelectrochemical and Photocatalytic Studies. *Journal of Materials Chemistry A* **2014**, *2*, 637−644.
(37) Zhang, N.; Li, X.; Ye, H.; Chen, S.; Ju, H.; Liu, D.; Lin, Y.; Ye, W.; Wang, C.; Xu, Q.; Zhu, J.; Song, L.; Jiang, J.; Xiong, Y. Oxide Defect Engineering Enables to Couple Solar Energy into Oxygen Activation. *J. Am. Chem. Soc.* **2016**, *138*, 8928−8935.
(38) Hu, J.; Zhao, X.; Chen, W.; Su, H.; Chen, Z. Theoretical Insight into the Mechanism of Photoelectrochemical Oxygen Evolution Reaction on $BiVO_4$ Anode with Oxygen Vacancy. *J. Phys. Chem. C* **2017**, *121*, 18702−18709.
(39) Wu, J.; Li, X.; Shi, W.; Ling, P.; Sun, Y.; Jiao, X.; Gao, S.; Liang, L.; Xu, J.; Yan, W.; Wang, C.; Xie, Y. Efficient Visible-Light-Driven CO_2 Reduction Mediated by Defect-Engineered BiOBr Atomic Layers. *Angew. Chem., Int. Ed.* **2018**, *57*, 8719−8723.
(40) Yu, J.; Kudo, A. Effects of Structural Variation on the Photocatalytic Performance of Hydrothermally Synthesized $BiVO_4$. *Adv. Funct. Mater.* **2006**, *16*, 2163−2169.
(41) Ye, L.; Zan, L.; Tian, L.; Peng, T.; Zhang, J. The {001} Facets-Dependent High Photoactivity of BiOCl Nanosheets. *Chem. Commun.* **2011**, *47*, 6951−6953.
(42) Ruberu, T. P. A.; Nelson, N. C.; Slowing, I. I.; Vela, J. Selective Alcohol Dehydrogenation and Hydrogenolysis with Semiconductor-Metal Photocatalysts: Toward Solar-to-Chemical Energy Conversion of Biomass-Relevant Substrates. *J. Phys. Chem. Lett.* **2012**, *3*, 2798−2802.
(43) Zhu, W.; Michalsky, R.; Metin, Ö.; Lv, H.; Guo, S.; Wright, C. J.; Sun, X.; Peterson, A. A.; Sun, S. Monodisperse Au Nanoparticles for Selective Electrocatalytic Reduction of CO_2 to CO. *J. Am. Chem. Soc.* **2013**, *135*, 16833−16836.
(44) Martin, D. J.; Umezawa, N.; Chen, X.; Ye, J.; Tang, J. Facet Engineered Ag_3PO_4 for Efficient Water Photooxidation. *Energy Environ. Sci.* **2013**, *6*, 3380−3386.
(45) Park, Y.; McDonald, K. J.; Choi, K.-S. Progress in Bismuth Vanadate Photoanodes for Use in Solar Water Oxidation. *Chem. Soc. Rev.* **2013**, *42*, 2321−2337.
(46) Yu, J.; Low, J.; Xiao, W.; Zhou, P.; Jaroniec, M. Enhanced Photocatalytic CO_2-Reduction Activity of Anatase TiO_2 by Coexposed {001} and {101} Facets. *J. Am. Chem. Soc.* **2014**, *136*, 8839−8842.
(47) Callejas, J. F.; McEnaney, J. M.; Read, C. G.; Crompton, J. C.; Biacchi, A. J.; Popczun, E. J.; Gordon, T. R.; Lewis, N. S.; Schaak, R. E. Electrocatalytic and Photocatalytic Hydrogen Production from Acidic and Neutral-pH Aqueous Solutions Using Iron Phosphide Nanoparticles. *ACS Nano* **2014**, *8*, 11101−11107.
(48) Zhu, W.; Shen, M.; Fan, G.; Yang, A.; Meyer, J. R.; Ou, Y.; Yin, B.; Fortner, J.; Foston, M.; Li, Z.; Zou, Z.; Sadtler, B. Facet-Dependent Enhancement in the Activity of Bismuth Vanadate Microcrystals for the Photocatalytic Conversion of Methane to Methanol. *ACS Applied Nano Materials* **2018**, *1*, 6683−6691.
(49) Lu, X.; Zeng, Y.; Yu, M.; Zhai, T.; Liang, C.; Xie, S.; Balogun, M.-S.; Tong, Y. Oxygen-Deficient Hematite Nanorods as High-Performance and Novel Negative Electrodes for Flexible Asymmetric Supercapacitors. *Adv. Mater.* **2014**, *26*, 3148−3155.
(50) Zhang, Y.; Guo, L.; Tao, L.; Lu, Y.; Wang, S. Defect-Based Single-Atom Electrocatalysts. *Small Methods* **2019**, *3*, 1800406.
(51) Zhang, S.; Si, Y.; Li, B.; Yang, L.; Dai, W.; Luo, S. Atomic-Level and Modulated Interfaces of Photocatalyst Heterostructure Constructed by External Defect-Induced Strategy: A Critical Review. *Small* **2021**, *17*, 2004980.
(52) Easter, Q. T.; Blum, S. A. Kinetics of the Same Reaction Monitored over Nine Orders of Magnitude in Concentration: When Are Unique Subensemble and Single-Turnover Reactivity Displayed? *Angew. Chem., Int. Ed.* **2018**, *57*, 12027−12032.
(53) Xu, W.; Kong, J. S.; Yeh, Y.-T. E.; Chen, P. Single-Molecule Nanocatalysis Reveals Heterogeneous Reaction Pathways and Catalytic Dynamics. *Nat. Mater.* **2008**, *7*, 992−996.
(54) Zhou, X.; Andoy, N. M.; Liu, G.; Choudhary, E.; Han, K.-S.; Shen, H.; Chen, P. Quantitative Super-Resolution Imaging Uncovers Reactivity Patterns on Single Nanocatalysts. *Nat. Nanotechnol.* **2012**, *7*, 237−241.
(55) Shen, M.; Ding, T.; Rackers, W. H.; Tan, C.; Mahmood, K.; Lew, M. D.; Sadtler, B. Single-Molecule Colocalization of Redox Reactions on Semiconductor Photocatalysts Connects Surface Heterogeneity and Charge-Carrier Separation in Bismuth Oxybromide. *J. Am. Chem. Soc.* **2021**, *143*, 11393−11403.
(56) Erickson, E. M.; Thorum, M. S.; Vasić, R.; Marinković, N. S.; Frenkel, A. I.; Gewirth, A. A.; Nuzzo, R. G. In Situ Electrochemical X-Ray Absorption Spectroscopy of Oxygen Reduction Electrocatalysis with High Oxygen Flux. *J. Am. Chem. Soc.* **2012**, *134*, 197−200.
(57) May, K. J.; Carlton, C. E.; Stoerzinger, K. A.; Risch, M.; Suntivich, J.; Lee, Y.-L.; Grimaud, A.; Shao-Horn, Y. Influence of Oxygen Evolution During Water Oxidation on the Surface of Perovskite Oxide Catalysts. *J. Phys. Chem. Lett.* **2012**, *3*, 3264−3270.
(58) Liu, L.; Meira, D. M.; Arenal, R.; Concepcion, P.; Puga, A. V.; Corma, A. Determination of the Evolution of Heterogeneous Single Metal Atoms and Nanoclusters under Reaction Conditions: Which Are the Working Catalytic Sites? *ACS Catal.* **2019**, *9*, 10626−10639.
(59) Hochfilzer, D.; Chorkendorff, I.; Kibsgaard, J. Catalyst Stability Considerations for Electrochemical Energy Conversion with Non-Noble Metals: Do We Measure on What We Synthesized? *ACS Energy Letters* **2023**, *8*, 1607−1612.
(60) Roeffaers, M. B. J.; Sels, B. F.; Uji-i, H.; De Schryver, F. C.; Jacobs, P. A.; De Vos, D. E.; Hofkens, J. Spatially Resolved Observation of Crystal-Face-Dependent Catalysis by Single Turnover Counting. *Nature* **2006**, *439*, 572−575.
(61) Roeffaers, M. B. J.; Sels, B. F.; Uji-i, H.; Blanpain, B.; L'hoëst, P.; Jacobs, P. A.; De Schryver, F. C.; Hofkens, J.; De Vos, D. E. Space- and Time-Resolved Visualization of Acid Catalysis in ZSM-5 Crystals by Fluorescence Microscopy. *Angew. Chem., Int. Ed.* **2007**, *46*, 1706−1709.
(62) Roeffaers, M. B. J.; De Cremer, G.; Libeert, J.; Ameloot, R.; Dedecker, P.; Bons, A.-J.; Bückins, M.; Martens, J. A.; Sels, B. F.; De Vos, D. E.; Hofkens, J. Super-Resolution Reactivity Mapping of Nanostructured Catalyst Particles. *Angew. Chem., Int. Ed.* **2009**, *48*, 9285−9289.
(63) De Cremer, G.; Roeffaers, M. B. J.; Bartholomeeusen, E.; Lin, K.; Dedecker, P.; Pescarmona, P. P.; Jacobs, P. A.; De Vos, D. E.; Hofkens, J.; Sels, B. F. High-Resolution Single-Turnover Mapping Reveals Intraparticle Diffusion Limitation in Ti-MCM-41-Catalyzed Epoxidation. *Angew. Chem., Int. Ed.* **2010**, *49*, 908−911.
(64) Xu, W.; Kong, J. S.; Chen, P. Probing the Catalytic Activity and Heterogeneity of Au-Nanoparticles at the Single-Molecule Level. *Phys. Chem. Chem. Phys.* **2009**, *11*, 2767−2778.
(65) Zhou, X.; Xu, W.; Liu, G.; Panda, D.; Chen, P. Size-Dependent Catalytic Activity and Dynamics of Gold Nanoparticles at the Single-Molecule Level. *J. Am. Chem. Soc.* **2010**, *132*, 138−146.
(66) Han, K. S.; Liu, G.; Zhou, X.; Medina, R. E.; Chen, P. How Does a Single Pt Nanocatalyst Behave in Two Different Reactions? A Single-Molecule Study. *Nano Lett.* **2012**, *12*, 1253−1259.

https://doi.org/10.1021/cbmi.3c00075
Chem. Biomed. Imaging 2023, 1, 692−715

(67) Naito, K.; Tachikawa, T.; Fujitsuka, M.; Majima, T. Single-Molecule Fluorescence Imaging of the Remote TiO_2 Photocatalytic Oxidation. *J. Phys. Chem. B* **2005**, *109*, 23138−23140.
(68) Naito, K.; Tachikawa, T.; Cui, S.-C.; Sugimoto, A.; Fujitsuka, M.; Majima, T. Single-Molecule Detection of Airborne Singlet Oxygen. *J. Am. Chem. Soc.* **2006**, *128*, 16430−16431.
(69) Naito, K.; Tachikawa, T.; Fujitsuka, M.; Majima, T. Real-Time Single-Molecule Imaging of the Spatial and Temporal Distribution of Reactive Oxygen Species with Fluorescent Probes: Applications to TiO_2 Photocatalysts. *J. Phys. Chem. C* **2008**, *112*, 1048−1059.
(70) Dong, B.; Pei, Y.; Zhao, F.; Goh, T. W.; Qi, Z.; Xiao, C.; Chen, K.; Huang, W.; Fang, N. In Situ Quantitative Single-Molecule Study of Dynamic Catalytic Processes in Nanoconfinement. *Nature Catalysis* **2018**, *1*, 135−140.
(71) Dong, B.; Pei, Y.; Mansour, N.; Lu, X.; Yang, K.; Huang, W.; Fang, N. Deciphering Nanoconfinement Effects on Molecular Orientation and Reaction Intermediate by Single Molecule Imaging. *Nat. Commun.* **2019**, *10*, 4815.
(72) Dong, B.; Mansour, N.; Pei, Y.; Wang, Z.; Huang, T.; Filbrun, S. L.; Chen, M.; Cheng, X.; Pruski, M.; Huang, W.; Fang, N. Single Molecule Investigation of Nanoconfinement Hydrophobicity in Heterogeneous Catalysis. *J. Am. Chem. Soc.* **2020**, *142*, 13305−13309.
(73) Wang, N.; Tachikawa, T.; Majima, T. Single-Molecule, Single-Particle Observation of Size-Dependent Photocatalytic Activity in Au/TiO_2 Nanocomposites. *Chemical Science* **2011**, *2*, 891−900.
(74) Tachikawa, T.; Yonezawa, T.; Majima, T. Super-Resolution Mapping of Reactive Sites on Titania-Based Nanoparticles with Water-Soluble Fluorogenic Probes. *ACS Nano* **2013**, *7*, 263−275.
(75) Ha, J. W.; Ruberu, T. P. A.; Han, R.; Dong, B.; Vela, J.; Fang, N. Super-Resolution Mapping of Photogenerated Electron and Hole Separation in Single Metal-Semiconductor Nanocatalysts. *J. Am. Chem. Soc.* **2014**, *136*, 1398−1408.
(76) Sambur, J. B.; Chen, T.-Y.; Choudhary, E.; Chen, G.; Nissen, E. J.; Thomas, E. M.; Zou, N.; Chen, P. Sub-Particle Reaction and Photocurrent Mapping to Optimize Catalyst-Modified Photoanodes. *Nature* **2016**, *530*, 77−80.
(77) Liu, Y.; Zhang, K.; Tian, X.; Zhou, L.; Liu, J.; Liu, B. Quantitative Single-Particle Fluorescence Imaging Elucidates Semiconductor Shell Influence on Ag@TiO_2 Photocatalysis. *ACS Appl. Mater. Interfaces* **2021**, *13*, 7680−7687.
(78) An, J.; Song, X.; Wan, W.; Chen, Y.; Si, H.; Duan, H.; Li, L.; Tang, B. Kinetics of the Photoelectron-Transfer Process Characterized by Real-Time Single-Molecule Fluorescence Imaging on Individual Photocatalyst Particles. *ACS Catal.* **2021**, *11*, 6872−6882.
(79) Wu, S.; Lee, J.-K.; Lim, P. C.; Xu, R.; Zhang, Z. Super-Resolution Imaging of Photogenerated Charges on CdS/g-C_3N_4 Heterojunctions and Its Correlation with Photoactivity. *Nanoscale* **2022**, *14*, 5612−5624.
(80) Andoy, N. M.; Zhou, X.; Choudhary, E.; Shen, H.; Liu, G.; Chen, P. Single-Molecule Catalysis Mapping Quantifies Site-Specific Activity and Uncovers Radial Activity Gradient on Single 2D Nanocrystals. *J. Am. Chem. Soc.* **2013**, *135*, 1845−1852.
(81) Shen, M.; Ding, T.; Hartman, S. T.; Wang, F.; Krucylak, C.; Wang, Z.; Tan, C.; Yin, B.; Mishra, R.; Lew, M. D.; Sadtler, B. Nanoscale Colocalization of Fluorogenic Probes Reveals the Role of Oxygen Vacancies in the Photocatalytic Activity of Tungsten Oxide Nanowires. *ACS Catal.* **2020**, *10*, 2088−2099.
(82) Shen, M.; Ding, T.; Luo, J.; Tan, C.; Mahmood, K.; Wang, Z.; Zhang, D.; Mishra, R.; Lew, M. D.; Sadtler, B. Competing Activation and Deactivation Mechanisms in Photodoped Bismuth Oxybromide Nanoplates Probed by Single-Molecule Fluorescence Imaging. *J. Phys. Chem. Lett.* **2020**, *11*, 5219−5227.
(83) Shen, M.; Ding, T.; Tan, C.; Rackers, W. H.; Zhang, D.; Lew, M. D.; Sadtler, B. In Situ Imaging of Catalytic Reactions on Tungsten Oxide Nanowires Connects Surface-Ligand Redox Chemistry with Photocatalytic Activity. *Nano Lett.* **2022**, *22*, 4694−4701.
(84) Huang, T.-X.; Dong, B.; Filbrun, S. L.; Okmi, A. A.; Cheng, X.; Yang, M.; Mansour, N.; Lei, S.; Fang, N. Single-Molecule Photocatalytic Dynamics at Individual Defects in Two-Dimensional Layered Materials. *Science Advances* **2021**, *7*, No. eabj4452.
(85) Xu, W.; Shen, H.; Kim, Y. J.; Zhou, X.; Liu, G.; Park, J.; Chen, P. Single-Molecule Electrocatalysis by Single-Walled Carbon Nanotubes. *Nano Lett.* **2009**, *9*, 3968−3973.
(86) Xu, W.; Jain, P. K.; Beberwyck, B. J.; Alivisatos, A. P. Probing Redox Photocatalysis of Trapped Electrons and Holes on Single Sb-Doped Titania Nanorod Surfaces. *J. Am. Chem. Soc.* **2012**, *134*, 3946−3949.
(87) Tachikawa, T.; Yamashita, S.; Majima, T. Evidence for Crystal-Face-Dependent TiO_2 Photocatalysis from Single-Molecule Imaging and Kinetic Analysis. *J. Am. Chem. Soc.* **2011**, *133*, 7197−7204.
(88) Zhou, X.; Choudhary, E.; Andoy, N. M.; Zou, N.; Chen, P. Scalable Parallel Screening of Catalyst Activity at the Single-Particle Level and Subdiffraction Resolution. *ACS Catal.* **2013**, *3*, 1448−1453.
(89) Zhang, Y.; Lucas, J. M.; Song, P.; Beberwyck, B.; Fu, Q.; Xu, W.; Alivisatos, A. P. Superresolution Fluorescence Mapping of Single-Nanoparticle Catalysts Reveals Spatiotemporal Variations in Surface Reactivity. *Proc. Natl. Acad. Sci. U. S. A.* **2015**, *112*, 8959−8964.
(90) Chen, T.; Zhang, Y.; Xu, W. Single-Molecule Nanocatalysis Reveals Catalytic Activation Energy of Single Nanocatalysts. *J. Am. Chem. Soc.* **2016**, *138*, 12414−12421.
(91) Chen, T.; Dong, B.; Chen, K.; Zhao, F.; Cheng, X.; Ma, C.; Lee, S.; Zhang, P.; Kang, S. H.; Ha, J. W.; Xu, W.; Fang, N. Optical Super-Resolution Imaging of Surface Reactions. *Chem. Rev.* **2017**, *117*, 7510−7537.
(92) Chen, T.; Chen, S.; Song, P.; Zhang, Y.; Su, H.; Xu, W.; Zeng, J. Single-Molecule Nanocatalysis Reveals Facet-Dependent Catalytic Kinetics and Dynamics of Pallidium Nanoparticles. *ACS Catal.* **2017**, *7*, 2967−2972.
(93) Zou, N.; Chen, G.; Mao, X.; Shen, H.; Choudhary, E.; Zhou, X.; Chen, P. Imaging Catalytic Hotspots on Single Plasmonic Nanostructures via Correlated Super-Resolution and Electron Microscopy. *ACS Nano* **2018**, *12*, 5570−5579.
(94) Zou, N.; Zhou, X.; Chen, G.; Andoy, N. M.; Jung, W.; Liu, G.; Chen, P. Cooperative Communication within and between Single Nanocatalysts. *Nat. Chem.* **2018**, *10*, 607−614.
(95) Hesari, M.; Mao, X.; Chen, P. Charge Carrier Activity on Single-Particle Photo(Electro)Catalysts: Toward Function in Solar Energy Conversion. *J. Am. Chem. Soc.* **2018**, *140*, 6729−6740.
(96) Mao, X.; Liu, C.; Hesari, M.; Zou, N.; Chen, P. Super-Resolution Imaging of Non-Fluorescent Reactions via Competition. *Nat. Chem.* **2019**, *11*, 687−694.
(97) Wang, W.-K.; Chen, J.-J.; Lou, Z.-Z.; Kim, S.; Fujitsuka, M.; Yu, H.-Q.; Majima, T. Single-Molecule and -Particle Probing Crystal Edge/Corner as Highly Efficient Photocatalytic Sites on a Single TiO_2 Particle. *Proc. Natl. Acad. Sci. U. S. A.* **2019**, *116*, 18827−18833.
(98) Ye, R.; Zhao, M.; Mao, X.; Wang, Z.; Garzón, D. A.; Pu, H.; Zhao, Z.; Chen, P. Nanoscale Cooperative Adsorption for Materials Control. *Nat. Commun.* **2021**, *12*, 4287.
(99) Liu, X.; Ge, X.; Cao, J.; Xiao, Y.; Wang, Y.; Zhang, W.; Song, P.; Xu, W. Revealing the Catalytic Kinetics and Dynamics of Individual Pt Atoms at the Single-Molecule Level. *Proc. Natl. Acad. Sci. U. S. A.* **2022**, *119*, No. e2114639119.
(100) Mao, X.; Chen, P. Inter-Facet Junction Effects on Particulate Photoelectrodes. *Nat. Mater.* **2022**, *21*, 331−337.
(101) Lustig, D. R.; Nilsson, Z. N.; Mulvey, J. T.; Zang, W.; Pan, X.; Patterson, J. P.; Sambur, J. B. Toward Imaging Defect-Mediated Energy Transfer between Single Nanocrystal Donors and Single Molecule Acceptors. *Chemical & Biomedical Imaging* **2023**, *1*, 168−178.
(102) Wilson, A. J.; Willets, K. A. Visualizing Site-Specific Redox Potentials on the Surface of Plasmonic Nanoparticle Aggregates with Superlocalization SERS Microscopy. *Nano Lett.* **2014**, *14*, 939−945.
(103) Willets, K. A.; Wilson, A. J.; Sundaresan, V.; Joshi, P. B. Super-Resolution Imaging and Plasmonics. *Chem. Rev.* **2017**, *117*, 7538−7582.
(104) Easter, Q. T.; Garcia IV, A.; Blum, S. A. Single-Polymer-Particle Growth Kinetics with Molecular Catalyst Speciation and Single-Turnover Imaging. *ACS Catal.* **2019**, *9*, 3375−3383.

https://doi.org/10.1021/cbmi.3c00075
Chem. Biomed. Imaging 2023, 1, 692−715

(105) Garcia IV, A.; Saluga, S. J.; Dibble, D. J.; López, P. A.; Saito, N.; Blum, S. A. Does Selectivity of Molecular Catalysts Change with Time? Polymerization Imaged by Single-Molecule Spectroscopy. *Angew. Chem., Int. Ed.* **2021**, *60*, 1550−1555.
(106) Eivgi, O.; Blum, S. A. Exploring Chemistry with Single-Molecule and -Particle Fluorescence Microscopy. *Trends in Chemistry* **2022**, *4*, 5−14.
(107) Matsushima, H.; Taranovskyy, A.; Haak, C.; Gründer, Y.; Magnussen, O. M. Reconstruction of Cu(100) Electrode Surfaces During Hydrogen Evolution. *J. Am. Chem. Soc.* **2009**, *131*, 10362−10363.
(108) Parkinson, G. S.; Novotny, Z.; Argentero, G.; Schmid, M.; Pavelec, J.; Kosak, R.; Blaha, P.; Diebold, U. Carbon Monoxide-Induced Adatom Sintering in a Pd-Fe_3O_4 Model Catalyst. *Nat. Mater.* **2013**, *12*, 724−728.
(109) Kim, Y.-G.; Baricuatro, J. H.; Javier, A.; Gregoire, J. M.; Soriaga, M. P. The Evolution of the Polycrystalline Copper Surface, First to Cu(111) and Then to Cu(100), at a Fixed CO_2RR Potential: A Study by *Operando* EC-STM. *Langmuir* **2014**, *30*, 15053−15056.
(110) Kudernatsch, W.; Peng, G.; Zeuthen, H.; Bai, Y.; Merte, L. R.; Lammich, L.; Besenbacher, F.; Mavrikakis, M.; Wendt, S. Direct Visualization of Catalytically Active Sites at the FeO-Pt(111) Interface. *ACS Nano* **2015**, *9*, 7804−7814.
(111) Wintterlin, J.; Völkening, S.; Janssens, T. V. W.; Zambelli, T.; Ertl, G. Atomic and Macroscopic Reaction Rates of a Surface-Catalyzed Reaction. *Science* **1997**, *278*, 1931−1934.
(112) Mitsui, T.; Rose, M. K.; Fomin, E.; Ogletree, D. F.; Salmeron, M. Dissociative Hydrogen Adsorption on Palladium Requires Aggregates of Three or More Vacancies. *Nature* **2003**, *422*, 705−707.
(113) Matthiesen, J.; Wendt, S.; Hansen, J. Ø.; Madsen, G. K. H.; Lira, E.; Galliker, P.; Vestergaard, E. K.; Schaub, R.; Lægsgaard, E.; Hammer, B.; Besenbacher, F. Observation of All the Intermediate Steps of a Chemical Reaction on an Oxide Surface by Scanning Tunneling Microscopy. *ACS Nano* **2009**, *3*, 517−526.
(114) Pfisterer, J. H. K.; Liang, Y.; Schneider, O.; Bandarenka, A. S. Direct Instrumental Identification of Catalytically Active Surface Sites. *Nature* **2017**, *549*, 74−77.
(115) Han, W.; Durantini, E. N.; Moore, T. A.; Moore, A. L.; Gust, D.; Rez, P.; Leatherman, G.; Seely, G. R.; Tao, N.; Lindsay. STM Contrast, Electron-Transfer Chemistry, and Conduction in Molecules. *J. Phys. Chem. B* **1997**, *101*, 10719−10725.
(116) Tsoi, S.; Griva, I.; Trammell, S. A.; Blum, A. S.; Schnur, J. M.; Lebedev, N. Electrochemically Controlled Conductance Switching in a Single Molecule: Quinone-Modified Oligo(Phenylene Vinylene). *ACS Nano* **2008**, *2*, 1289−1295.
(117) Yuan, Q.; Xing, Y.; Borguet, E. An STM Study of the pH Dependent Redox Activity of a Two-Dimensional Hydrogen Bonding Porphyrin Network at an Electrochemical Interface. *J. Am. Chem. Soc.* **2010**, *132*, 5054−5060.
(118) Chen, T.; Wang, D.; Gan, L.-H.; Matsuo, Y.; Gu, J.-Y.; Yan, H.-J.; Nakamura, E.; Wan, L.-J. Direct Probing of the Structure and Electron Transfer of Fullerene/Ferrocene Hybrid on Au(111) Electrodes by in Situ Electrochemical STM. *J. Am. Chem. Soc.* **2014**, *136*, 3184−3191.
(119) van Schrojenstein Lantman, E. M.; Deckert-Gaudig, T.; Mank, A. J. G.; Deckert, V.; Weckhuysen, B. M. Catalytic Processes Monitored at the Nanoscale with Tip-Enhanced Raman Spectroscopy. *Nat. Nanotechnol.* **2012**, *7*, 583−586.
(120) Kurouski, D.; Mattei, M.; Van Duyne, R. P. Probing Redox Reactions at the Nanoscale with Electrochemical Tip-Enhanced Raman Spectroscopy. *Nano Lett.* **2015**, *15*, 7956−7962.
(121) Kumar, N.; Stephanidis, B.; Zenobi, R.; Wain, A. J.; Roy, D. Nanoscale Mapping of Catalytic Activity Using Tip-Enhanced Raman Spectroscopy. *Nanoscale* **2015**, *7*, 7133−7137.
(122) Zeng, Z.-C.; Huang, S.-C.; Wu, D.-Y.; Meng, L.-Y.; Li, M.-H.; Huang, T.-X.; Zhong, J.-H.; Wang, X.; Yang, Z.-L.; Ren, B. Electrochemical Tip-Enhanced Raman Spectroscopy. *J. Am. Chem. Soc.* **2015**, *137*, 11928−11931.
(123) Pfisterer, J. H. K.; Baghernejad, M.; Giuzio, G.; Domke, K. F. Reactivity Mapping of Nanoscale Defect Chemistry under Electrochemical Reaction Conditions. *Nat. Commun.* **2019**, *10*, 5702.
(124) Yin, H.; Zheng, L.-Q.; Fang, W.; Lai, Y.-H.; Porenta, N.; Goubert, G.; Zhang, H.; Su, H.-S.; Ren, B.; Richardson, J. O.; Li, J.-F.; Zenobi, R. Nanometre-Scale Spectroscopic Visualization of Catalytic Sites During a Hydrogenation Reaction on a Pd/Au Bimetallic Catalyst. *Nature Catalysis* **2020**, *3*, 834−842.
(125) Tao, F.; Crozier, P. A. Atomic-Scale Observations of Catalyst Structures under Reaction Conditions and During Catalysis. *Chem. Rev.* **2016**, *116*, 3487−3539.
(126) Wu, J.; Shan, H.; Chen, W.; Gu, X.; Tao, P.; Song, C.; Shang, W.; Deng, T. In Situ Environmental TEM in Imaging Gas and Liquid Phase Chemical Reactions for Materials Research. *Adv. Mater.* **2016**, *28*, 9686−9712.
(127) Hwang, S.; Chen, X.; Zhou, G.; Su, D. In Situ Transmission Electron Microscopy on Energy-Related Catalysis. *Adv. Energy Mater.* **2020**, *10*, 1902105.
(128) He, B.; Zhang, Y.; Liu, X.; Chen, L. In-Situ Transmission Electron Microscope Techniques for Heterogeneous Catalysis. *ChemCatChem.* **2020**, *12*, 1853−1872.
(129) Ye, F.; Xu, M.; Dai, S.; Tieu, P.; Ren, X.; Pan, X. In Situ TEM Studies of Catalysts Using Windowed Gas Cells. *Catalysts* **2020**, *10*, 779.
(130) Chenna, S.; Banerjee, R.; Crozier, P. A. Atomic-Scale Observation of the Ni Activation Process for Partial Oxidation of Methane Using In Situ Environmental TEM. *ChemCatChem.* **2011**, *3*, 1051−1059.
(131) Chenna, S.; Crozier, P. A. Operando Transmission Electron Microscopy: A Technique for Detection of Catalysis Using Electron Energy-Loss Spectroscopy in the Transmission Electron Microscope. *ACS Catal.* **2012**, *2*, 2395−2402.
(132) Vendelbo, S. B.; Elkjær, C. F.; Falsig, H.; Puspitasari, I.; Dona, P.; Mele, L.; Morana, B.; Nelissen, B. J.; van Rijn, R.; Creemer, J. F.; Kooyman, P. J.; Helveg, S. Visualization of Oscillatory Behaviour of Pt Nanoparticles Catalysing CO Oxidation. *Nat. Mater.* **2014**, *13*, 884−890.
(133) Miller, B. K.; Crozier, P. A. Linking Changes in Reaction Kinetics and Atomic-Level Surface Structures on a Supported Ru Catalyst for CO Oxidation. *ACS Catal.* **2021**, *11*, 1456−1463.
(134) De Vrieze, J. E.; Bremmer, G. M.; Aly, M.; Navarro, V.; Thybaut, J. W.; Kooyman, P. J.; Saeys, M. Shape of Cobalt and Platinum Nanoparticles under a CO Atmosphere: A Combined In Situ TEM and Computational Catalysis Study. *ACS Catal.* **2019**, *9*, 7449−7456.
(135) Lee, J.; Kang, S.; Lee, E.; Kang, M.; Sung, J.; Kim, T. J.; Christopher, P.; Park, J.; Kim, D. H. Aggregation of CeO_2 Particles with Aligned Grains Drives Sintering of Pt Single Atoms in Pt/CeO_2 Catalysts. *Journal of Materials Chemistry A* **2022**, *10*, 7029−7035.
(136) Huang, J. Y.; Zhong, L.; Wang, C. M.; Sullivan, J. P.; Xu, W.; Zhang, L. Q.; Mao, S. X.; Hudak, N. S.; Liu, X. H.; Subramanian, A.; Fan, H.; Qi, L.; Kushima, A.; Li, J. In Situ Observation of the Electrochemical Lithiation of a Single SnO_2 Nanowire Electrode. *Science* **2010**, *330*, 1515−1520.
(137) McDowell, M. T.; Lee, S. W.; Harris, J. T.; Korgel, B. A.; Wang, C.; Nix, W. D.; Cui, Y. In Situ TEM of Two-Phase Lithiation of Amorphous Silicon Nanospheres. *Nano Lett.* **2013**, *13*, 758−764.
(138) Sun, M.; Liao, H.-G.; Niu, K.; Zheng, H. Structural and Morphological Evolution of Lead Dendrites During Electrochemical Migration. *Sci. Rep.* **2013**, *3*, 3227.
(139) Park, H.; Jeon, Y.; Chung, W. J.; Bae, Y.; Kim, J.; Baek, H.; Park, J. Early Stage Li Plating by Liquid Phase and Cryogenic Transmission Electron Microscopy. *ACS Energy Letters* **2023**, *8*, 715−721.
(140) Ortiz Peña, N.; Ihiawakrim, D.; Han, M.; Lassalle-Kaiser, B.; Carenco, S.; Sanchez, C.; Laberty-Robert, C.; Portehault, D.; Ersen, O. Morphological and Structural Evolution of Co_3O_4 Nanoparticles Revealed by *in Situ* Electrochemical Transmission Electron Microscopy During Electrocatalytic Water Oxidation. *ACS Nano* **2019**, *13*, 11372−11381.

https://doi.org/10.1021/cbmi.3c00075
Chem. Biomed. Imaging 2023, 1, 692−715

(141) Sun, H.; Liu, Q.; Gao, Z.; Geng, L.; Li, Y.; Zhang, F.; Yan, J.; Gao, Y.; Suenaga, K.; Zhang, L.; Tang, Y.; Huang, J. In Situ TEM Visualization of Single Atom Catalysis in Solid-State Na-O_2 Nanobatteries. *Journal of Materials Chemistry A* **2022**, *10*, 6096−6106.
(142) Zhang, L.; Miller, B. K.; Crozier, P. A. Atomic Level In Situ Observation of Surface Amorphization in Anatase Nanocrystals During Light Irradiation in Water Vapor. *Nano Lett.* **2013**, *13*, 679−684.
(143) Lu, Y.; Yin, W.-J.; Peng, K.-L.; Wang, K.; Hu, Q.; Selloni, A.; Chen, F.-R.; Liu, L.-M.; Sui, M.-L. Self-Hydrogenated Shell Promoting Photocatalytic H_2 Evolution on Anatase TiO_2. *Nat. Commun.* **2018**, *9*, 2752.
(144) Crozier, P. A.; Aoki, T.; Liu, Q. Detection of Water and Its Derivatives on Individual Nanoparticles Using Vibrational Electron Energy-Loss Spectroscopy. *Ultramicroscopy* **2016**, *169*, 30−36.
(145) Masliuk, L.; Swoboda, M.; Algara-Siller, G.; Schlögl, R.; Lunkenbein, T. A *quasi in situ* TEM Grid Reactor for Decoupling Catalytic Gas Phase Reactions and Analysis. *Ultramicroscopy* **2018**, *195*, 121−128.
(146) Kim, J.; Park, A.; Kim, J.; Kwak, S. J.; Lee, J. Y.; Lee, D.; Kim, S.; Choi, B. K.; Kim, S.; Kwag, J.; Kim, Y.; Jeon, S.; Lee, W. C.; Hyeon, T.; Lee, C.-H.; Lee, W. B.; Park, J. Observation of H_2 Evolution and Electrolyte Diffusion on MoS_2 Monolayer by In Situ Liquid-Phase Transmission Electron Microscopy. *Adv. Mater.* **2022**, *34*, 2206066.
(147) Yin, Z.-W.; Betzler, S. B.; Sheng, T.; Zhang, Q.; Peng, X.; Shangguan, J.; Bustillo, K. C.; Li, J.-T.; Sun, S.-G.; Zheng, H. Visualization of Facet-Dependent Pseudo-Photocatalytic Behavior of TiO_2 Nanorods for Water Splitting Using in Situ Liquid Cell TEM. *Nano Energy* **2019**, *62*, 507−512.
(148) Barroo, C.; Wang, Z.-J.; Schlögl, R.; Willinger, M.-G. Imaging the Dynamics of Catalysed Surface Reactions by in Situ Scanning Electron Microscopy. *Nature Catalysis* **2020**, *3*, 30−39.
(149) Bard, A. J.; Fan, F. R. F.; Kwak, J.; Lev, O. Scanning Electrochemical Microscopy. Introduction and Principles. *Anal. Chem.* **1989**, *61*, 132−138.
(150) Fernández, J. L.; White, J. M.; Sun, Y.; Tang, W.; Henkelman, G.; Bard, A. J. Characterization and Theory of Electrocatalysts Based on Scanning Electrochemical Microscopy Screening Methods. *Langmuir* **2006**, *22*, 10426−10431.
(151) Joshi, V. S.; Haram, S. K.; Dasgupta, A.; Kumar, G. V. P. Mapping of Electrocatalytic Sites on a Single Strand of Carbon Fiber Using Scanning Electrochemical Microscopy (SECM). *J. Phys. Chem. C* **2012**, *116*, 9703−9708.
(152) Li, H.; Du, M.; Mleczko, M. J.; Koh, A. L.; Nishi, Y.; Pop, E.; Bard, A. J.; Zheng, X. Kinetic Study of Hydrogen Evolution Reaction over Strained MoS_2 with Sulfur Vacancies Using Scanning Electrochemical Microscopy. *J. Am. Chem. Soc.* **2016**, *138*, 5123−5129.
(153) Mariano, R. G.; McKelvey, K.; White, H. S.; Kanan, M. W. Selective Increase in CO_2 Electroreduction Activity at Grain-Boundary Surface Terminations. *Science* **2017**, *358*, 1187−1192.
(154) Erdewyk, M. V.; Sambur, J. B. Single Nanoflake Photoelectrochemistry Reveals Intrananoflake Doping Heterogeneity That Explains Ensemble-Level Photoelectrochemical Behavior. *ACS Appl. Mater. Interfaces* **2022**, *14*, 22737−22746.
(155) Ye, H.; Lee, J.; Jang, J. S.; Bard, A. J. Rapid Screening of $BiVO_4$-Based Photocatalysts by Scanning Electrochemical Microscopy (SECM) and Studies of Their Photoelectrochemical Properties. *J. Phys. Chem. C* **2010**, *114*, 13322−13328.
(156) Aaronson, B. D. B.; Byers, J. C.; Colburn, A. W.; McKelvey, K.; Unwin, P. R. Scanning Electrochemical Cell Microscopy Platform for Ultrasensitive Photoelectrochemical Imaging. *Anal. Chem.* **2015**, *87*, 4129−4133.
(157) Bae, J. H.; Nepomnyashchii, A. B.; Wang, X.; Potapenko, D. V.; Mirkin, M. V. Photo-Scanning Electrochemical Microscopy on the Nanoscale with Through-Tip Illumination. *Anal. Chem.* **2019**, *91*, 12601−12605.
(158) Sarkar, S.; Wang, X.; Hesari, M.; Chen, P.; Mirkin, M. V. Scanning Electrochemical and Photoelectrochemical Microscopy on Finder Grids: Toward Correlative Multitechnique Imaging of Surfaces. *Anal. Chem.* **2021**, *93*, 5377−5382.
(159) Sun, T.; Wang, D.; Mirkin, M. V.; Cheng, H.; Zheng, J.-C.; Richards, R. M.; Lin, F.; Xin, H. L. Direct High-Resolution Mapping of Electrocatalytic Activity of Semi-Two-Dimensional Catalysts with Single-Edge Sensitivity. *Proc. Natl. Acad. Sci. U. S. A.* **2019**, *116*, 11618−11623.
(160) Kolagatla, S.; Subramanian, P.; Schechter, A. Catalytic Current Mapping of Oxygen Reduction on Isolated Pt Particles by Atomic Force Microscopy-Scanning Electrochemical Microscopy. *Applied Catalysis B: Environmental* **2019**, *256*, 117843.
(161) Snowden, M. E.; Güell, A. G.; Lai, S. C. S.; McKelvey, K.; Ebejer, N.; O'Connell, M. A.; Colburn, A. W.; Unwin, P. R. Scanning Electrochemical Cell Microscopy: Theory and Experiment for Quantitative High Resolution Spatially-Resolved Voltammetry and Simultaneous Ion-Conductance Measurements. *Anal. Chem.* **2012**, *84*, 2483−2491.
(162) Patten, H. V.; Lai, S. C. S.; Macpherson, J. V.; Unwin, P. R. Active Sites for Outer-Sphere, Inner-Sphere, and Complex Multistage Electrochemical Reactions at Polycrystalline Boron-Doped Diamond Electrodes (pBDD) Revealed with Scanning Electrochemical Cell Microscopy (SECCM). *Anal. Chem.* **2012**, *84*, 5427−5432.
(163) Bentley, C. L.; Kang, M.; Unwin, P. R. Nanoscale Structure Dynamics within Electrocatalytic Materials. *J. Am. Chem. Soc.* **2017**, *139*, 16813−16821.
(164) Wang, Y.; Li, M.; Ren, H. Voltammetric Mapping of Hydrogen Evolution Reaction on Pt Locally via Scanning Electrochemical Cell Microscopy. *ACS Measurement Science Au* **2022**, *2*, 304−308.
(165) Gossage, Z. T.; Schorr, N. B.; Hernández-Burgos, K.; Hui, J.; Simpson, B. H.; Montoto, E. C.; Rodríguez-López, J. Interrogating Charge Storage on Redox Active Colloids via Combined Raman Spectroscopy and Scanning Electrochemical Microscopy. *Langmuir* **2017**, *33*, 9455−9463.
(166) Schorr, N. B.; Jiang, A. G.; Rodríguez-López, J. Probing Graphene Interfacial Reactivity via Simultaneous and Colocalized Raman-Scanning Electrochemical Microscopy Imaging and Interrogation. *Anal. Chem.* **2018**, *90*, 7848−7854.
(167) Wang, Y.; Li, M.; Gordon, E.; Ye, Z.; Ren, H. Nanoscale Colocalized Electrochemical and Structural Mapping of Metal Dissolution Reaction. *Anal. Chem.* **2022**, *94*, 9058−9064.
(168) Grunwaldt, J.-D.; Schroer, C. G. Hard and Soft X-Ray Microscopy and Tomography in Catalysis: Bridging the Different Time and Length Scales. *Chem. Soc. Rev.* **2010**, *39*, 4741−4753.
(169) Kaulich, B.; Thibault, P.; Gianoncelli, A.; Kiskinova, M. Transmission and Emission X-Ray Microscopy: Operation Modes, Contrast Mechanisms and Applications. *J. Phys.: Condens. Matter* **2011**, *23*, 083002.
(170) Spence, S.; Lee, W.-K.; Lin, F.; Xiao, X. Transmission X-Ray Microscopy and Its Applications in Battery Material Research—a Short Review. *Nanotechnology* **2021**, *32*, 442003.
(171) Mefford, J. T.; Akbashev, A. R.; Kang, M.; Bentley, C. L.; Gent, W. E.; Deng, H. D.; Alsem, D. H.; Yu, Y.-S.; Salmon, N. J.; Shapiro, D. A.; Unwin, P. R.; Chueh, W. C. Correlative Operando Microscopy of Oxygen Evolution Electrocatalysts. *Nature* **2021**, *593*, 67−73.
(172) Park, J.; Zhao, H.; Kang, S. D.; Lim, K.; Chen, C.-C.; Yu, Y.-S.; Braatz, R. D.; Shapiro, D. A.; Hong, J.; Toney, M. F.; Bazant, M. Z.; Chueh, W. C. Fictitious Phase Separation in Li Layered Oxides Driven by Electro-Autocatalysis. *Nat. Mater.* **2021**, *20*, 991−999.
(173) Yang, W.; Eraky, H.; Zhang, C.; Hitchcock, A. P.; Zhitomirsky, I. Scanning Transmission X-Ray Microscopy Studies of Electrochemical Activation and Capacitive Behavior of Mn_3O_4 Supercapacitor Electrodes. *Journal of Materials Chemistry A* **2022**, *10*, 18267−18277.
(174) Zhao, H.; Deng, H. D.; Cohen, A. E.; Lim, J.; Li, Y.; Fraggedakis, D.; Jiang, B.; Storey, B. D.; Chueh, W. C.; Braatz, R. D.; Bazant, M. Z. Learning Heterogeneous Reaction Kinetics from X-Ray Videos Pixel by Pixel. *Nature* **2023**, *621*, 289−294.
(175) de Smit, E.; Swart, I.; Creemer, J. F.; Hoveling, G. H.; Gilles, M. K.; Tyliszczak, T.; Kooyman, P. J.; Zandbergen, H. W.; Morin, C.; Weckhuysen, B. M.; de Groot, F. M. F. Nanoscale Chemical Imaging of a Working Catalyst by Scanning Transmission X-Ray Microscopy. *Nature* **2008**, *456*, 222−225.

https://doi.org/10.1021/cbmi.3c00075
Chem. Biomed. Imaging 2023, 1, 692−715

(176) de Smit, E.; Swart, I.; Creemer, J. F.; Karunakaran, C.; Bertwistle, D.; Zandbergen, H. W.; de Groot, F. M. F.; Weckhuysen, B. M. Nanoscale Chemical Imaging of the Reduction Behavior of a Single Catalyst Particle. *Angew. Chem., Int. Ed.* **2009**, *48*, 3632−3636.
(177) Beheshti Askari, A.; al Samarai, M.; Morana, B.; Tillmann, L.; Pfänder, N.; Wandzilak, A.; Watts, B.; Belkhou, R.; Muhler, M.; DeBeer, S. In Situ X-Ray Microscopy Reveals Particle Dynamics in a NiCo Dry Methane Reforming Catalyst under Operating Conditions. *ACS Catal.* **2020**, *10*, 6223−6230.
(178) Zhang, C.; Shahcheraghi, L.; Ismail, F.; Eraky, H.; Yuan, H.; Hitchcock, A. P.; Higgins, D. Chemical Structure and Distribution in Nickel-Nitrogen-Carbon Catalysts for CO_2 Electroreduction Identified by Scanning Transmission X-Ray Microscopy. *ACS Catal.* **2022**, *12*, 8746−8760.
(179) Shapiro, D. A.; Yu, Y.-S.; Tyliszczak, T.; Cabana, J.; Celestre, R.; Chao, W.; Kaznatcheev, K.; Kilcoyne, A. L. D.; Maia, F.; Marchesini, S.; Meng, Y. S.; Warwick, T.; Yang, L. L.; Padmore, H. A. Chemical Composition Mapping with Nanometre Resolution by Soft X-Ray Microscopy. *Nat. Photonics* **2014**, *8*, 765−769.
(180) Yin, J.; Hu, Y.; Yoon, J. Fluorescent Probes and Bioimaging: Alkali Metals, Alkaline Earth Metals and pH. *Chem. Soc. Rev.* **2015**, *44*, 4619−4644.
(181) Chen, W.; Ma, X.; Chen, H.; Hua Liu, S.; Yin, J. Fluorescent Probes for pH and Alkali Metal Ions. *Coord. Chem. Rev.* **2021**, *427*, 213584.
(182) Chi, W.; Tan, D.; Qiao, Q.; Xu, Z.; Liu, X. Spontaneously Blinking Rhodamine Dyes for Single-Molecule Localization Microscopy. *Angew. Chem., Int. Ed.* **2023**, *62*, No. e202306061.
(183) Karaveli, S.; Gaathon, O.; Wolcott, A.; Sakakibara, R.; Shemesh, O. A.; Peterka, D. S.; Boyden, E. S.; Owen, J. S.; Yuste, R.; Englund, D. Modulation of Nitrogen Vacancy Charge State and Fluorescence in Nanodiamonds Using Electrochemical Potential. *Proc. Natl. Acad. Sci. U. S. A.* **2016**, *113*, 3938−3943.
(184) Dong, J.; Lu, Y.; Xu, Y.; Chen, F.; Yang, J.; Chen, Y.; Feng, J. Direct Imaging of Single-Molecule Electrochemical Reactions in Solution. *Nature* **2021**, *596*, 244−249.
(185) Fish, K. N. Total Internal Reflection Fluorescence (TIRF) Microscopy. *Current Protocols* **2022**, *2*, No. e517.
(186) Naito, K.; Tachikawa, T.; Fujitsuka, M.; Majima, T. Single-Molecule Observation of Photocatalytic Reaction in TiO_2 Nanotube: Importance of Molecular Transport through Porous Structures. *J. Am. Chem. Soc.* **2009**, *131*, 934−936.
(187) Tachikawa, T.; Wang, N.; Yamashita, S.; Cui, S.-C.; Majima, T. Design of a Highly Sensitive Fluorescent Probe for Interfacial Electron Transfer on a TiO_2 Surface. *Angew. Chem., Int. Ed.* **2010**, *49*, 8593−8597.
(188) Titus, E. J.; Willets, K. A. Superlocalization Surface-Enhanced Raman Scattering Microscopy: Comparing Point Spread Function Models in the Ensemble and Single-Molecule Limits. *ACS Nano* **2013**, *7*, 8284−8294.
(189) Fu, B.; Flynn, J. D.; Isaacoff, B. P.; Rowland, D. J.; Biteen, J. S. Super-Resolving the Distance-Dependent Plasmon-Enhanced Fluorescence of Single Dye and Fluorescent Protein Molecules. *J. Phys. Chem. C* **2015**, *119*, 19350−19358.
(190) Wertz, E.; Isaacoff, B. P.; Flynn, J. D.; Biteen, J. S. Single-Molecule Super-Resolution Microscopy Reveals How Light Couples to a Plasmonic Nanoantenna on the Nanometer Scale. *Nano Lett.* **2015**, *15*, 2662−2670.
(191) Su, L.; Yuan, H.; Lu, G.; Rocha, S.; Orrit, M.; Hofkens, J.; Uji-i, H. Super-Resolution Localization and Defocused Fluorescence Microscopy on Resonantly Coupled Single-Molecule, Single-Nanorod Hybrids. *ACS Nano* **2016**, *10*, 2455−2466.
(192) Rust, M. J.; Bates, M.; Zhuang, X. Sub-Diffraction-Limit Imaging by Stochastic Optical Reconstruction Microscopy (STORM). *Nat. Methods* **2006**, *3*, 793−796.
(193) Betzig, E.; Patterson, G. H.; Sougrat, R.; Lindwasser, O. W.; Olenych, S.; Bonifacino, J. S.; Davidson, M. W.; Lippincott-Schwartz, J.; Hess, H. F. Imaging Intracellular Fluorescent Proteins at Nanometer Resolution. *Science* **2006**, *313*, 1642−1645.
(194) Bates, M.; Huang, B.; Dempsey, G. T.; Zhuang, X. Multicolor Super-Resolution Imaging with Photo-Switchable Fluorescent Probes. *Science* **2007**, *317*, 1749−1753.
(195) Zhuang, X. Nano-Imaging with STORM. *Nat. Photonics* **2009**, *3*, 365−367.
(196) Schermelleh, L.; Heintzmann, R.; Leonhardt, H. A Guide to Super-Resolution Fluorescence Microscopy. *J. Cell Biol.* **2010**, *190*, 165−175.
(197) Yin, B.; Cavin, J.; Wang, D.; Khan, D.; Shen, M.; Laing, C.; Mishra, R.; Sadtler, B. Fluorescence Microscopy of Single Lead Bromide Nanocrystals Reveals Sharp Transitions During Their Transformation to Methylammonium Lead Bromide. *Journal of Materials Chemistry C* **2019**, *7*, 3486−3495.
(198) Wang, D.; Cavin, J.; Yin, B.; Thind, A. S.; Borisevich, A. Y.; Mishra, R.; Sadtler, B. Role of Solid-State Miscibility During Anion Exchange in Cesium Lead Halide Nanocrystals Probed by Single-Particle Fluorescence. *J. Phys. Chem. Lett.* **2020**, *11*, 952−959.
(199) Mills, A.; Wells, N.; MacKenzie, J.; MacDonald, G. Kinetics of Reduction of a Resazurin-Based Photocatalytic Activity Ink. *Catal. Today* **2017**, *281*, 14−20.
(200) Towne, V.; Will, M.; Oswald, B.; Zhao, Q. Complexities in Horseradish Peroxidase-Catalyzed Oxidation of Dihydroxyphenoxazine Derivatives: Appropriate Ranges for pH Values and Hydrogen Peroxide Concentrations in Quantitative Analysis. *Anal. Biochem.* **2004**, *334*, 290−296.
(201) Gatland, Z.; Madrid, D.; Siegel, M.; Kisley, L. Reduction Reactions at Metal/Non-Aqueous Interfaces Can Be Sensed with the Turn-on Fluorophore Resazurin. *Materials Chemistry Frontiers* **2023**, *7*, 2260−2265.
(202) Michel, B. W.; Lippert, A. R.; Chang, C. J. A Reaction-Based Fluorescent Probe for Selective Imaging of Carbon Monoxide in Living Cells Using a Palladium-Mediated Carbonylation. *J. Am. Chem. Soc.* **2012**, *134*, 15668−15671.
(203) Garcia IV, A.; Blum, S. A. Polymer Molecular Weight Determination via Fluorescence Lifetime. *J. Am. Chem. Soc.* **2022**, *144*, 22416−22420.
(204) Eivgi, O.; Blum, S. A. Real-Time Polymer Viscosity-Catalytic Activity Relationships on the Microscale. *J. Am. Chem. Soc.* **2022**, *144*, 13574−13585.
(205) Saluga, S. J.; Dibble, D. J.; Blum, S. A. Superresolved Motions of Single Molecular Catalysts During Polymerization Show Wide Distributions. *J. Am. Chem. Soc.* **2022**, *144*, 10591−10598.
(206) Zhou, M.; Diwu, Z.; Panchuk-Voloshina, N.; Haugland, R. P. A Stable Nonfluorescent Derivative of Resorufin for the Fluorometric Determination of Trace Hydrogen Peroxide: Applications in Detecting the Activity of Phagocyte NADPH Oxidase and Other Oxidases. *Anal. Biochem.* **1997**, *253*, 162−168.
(207) Gomes, A.; Fernandes, E.; Lima, J. L. F. C. Fluorescence Probes Used for Detection of Reactive Oxygen Species. *Journal of Biochemical and Biophysical Methods* **2005**, *65*, 45−80.
(208) Setsukinai, K.-i.; Urano, Y.; Kakinuma, K.; Majima, H. J.; Nagano, T. Development of Novel Fluorescence Probes That Can Reliably Detect Reactive Oxygen Species and Distinguish Specific Species. *J. Biol. Chem.* **2003**, *278*, 3170−3175.
(209) Kim, T.; Assary, R. S.; Kim, H.; Marshall, C. L.; Gosztola, D. J.; Curtiss, L. A.; Stair, P. C. Effects of Solvent on the Furfuryl Alcohol Polymerization Reaction: UV Raman Spectroscopy Study. *Catal. Today* **2013**, *205*, 60−66.
(210) Choura, M.; Belgacem, N. M.; Gandini, A. Acid-Catalyzed Polycondensation of Furfuryl Alcohol: Mechanisms of Chromophore Formation and Cross-Linking. *Macromolecules* **1996**, *29*, 3839−3850.
(211) Kim, T.; Assary, R. S.; Marshall, C. L.; Gosztola, D. J.; Curtiss, L. A.; Stair, P. C. Acid-Catalyzed Furfuryl Alcohol Polymerization: Characterizations of Molecular Structure and Thermodynamic Properties. *ChemCatChem.* **2011**, *3*, 1451−1458.
(212) Hendriks, F. C.; Mohammadian, S.; Ristanović, Z.; Kalirai, S.; Meirer, F.; Vogt, E. T. C.; Bruijnincx, P. C. A.; Gerritsen, H. C.; Weckhuysen, B. M. Integrated Transmission Electron and Single-Molecule Fluorescence Microscopy Correlates Reactivity with Ultra-

https://doi.org/10.1021/cbmi.3c00075
Chem. Biomed. Imaging 2023, 1, 692−715

structure in a Single Catalyst Particle. *Angew. Chem., Int. Ed.* **2018**, *57*, 257−261.
(213) Evans, R. C.; Ellingworth, A.; Cashen, C. J.; Weinberger, C. R.; Sambur, J. B. Influence of Single-Nanoparticle Electrochromic Dynamics on the Durability and Speed of Smart Windows. *Proc. Natl. Acad. Sci. U. S. A.* **2019**, *116*, 12666−12671.
(214) Jung, C.; Kirstein, J.; Platschek, B.; Bein, T.; Budde, M.; Frank, I.; Müllen, K.; Michaelis, J.; Bräuchle, C. Diffusion of Oriented Single Molecules with Switchable Mobility in Networks of Long Unidimensional Nanochannels. *J. Am. Chem. Soc.* **2008**, *130*, 1638−1648.
(215) Kumarasinghe, R.; Higgins, E. D.; Ito, T.; Higgins, D. A. Spectroscopic and Polarization-Dependent Single-Molecule Tracking Reveal the One-Dimensional Diffusion Pathways in Surfactant-Templated Mesoporous Silica. *J. Phys. Chem. C* **2016**, *120*, 715−723.
(216) Ding, T.; Wu, T.; Mazidi, H.; Zhang, O.; Lew, M. D. Single-Molecule Orientation Localization Microscopy for Resolving Structural Heterogeneities between Amyloid Fibrils. *Optica* **2020**, *7*, 602−607.
(217) Lu, J.; Mazidi, H.; Ding, T.; Zhang, O.; Lew, M. D. Single-Molecule 3D Orientation Imaging Reveals Nanoscale Compositional Heterogeneity in Lipid Membranes. *Angew. Chem., Int. Ed.* **2020**, *59*, 17572−17579.
(218) Liu, J.; Hill, C. M.; Pan, S.; Liu, H. Interfacial Charge Transfer Events of BODIPY Molecules: Single Molecule Spectroelectrochemistry and Substrate Effects. *Phys. Chem. Chem. Phys.* **2014**, *16*, 23150−23156.
(219) Ding, T.; Lew, M. D. Single-Molecule Localization Microscopy of 3D Orientation and Anisotropic Wobble Using a Polarized Vortex Point Spread Function. *J. Phys. Chem. B* **2021**, *125*, 12718−12729.
(220) Zhang, O.; Zhou, W.; Lu, J.; Wu, T.; Lew, M. D. Resolving the Three-Dimensional Rotational and Translational Dynamics of Single Molecules Using Radially and Azimuthally Polarized Fluorescence. *Nano Lett.* **2022**, *22*, 1024−1031.
(221) Fleischmann, S.; Spencer, M. A.; Augustyn, V. Electrochemical Reactivity under Confinement Enabled by Molecularly Pillared 2D and Layered Materials. *Chem. Mater.* **2020**, *32*, 3325−3334.
(222) Andronescu, C.; Masa, J.; Tilley, R. D.; Gooding, J. J.; Schuhmann, W. Electrocatalysis in Confined Space. *Current Opinion in Electrochemistry* **2021**, *25*, 100644.
(223) Creative Commons. https://creativecommons.org/licenses/by/4.0/ (accessed 06/15/2023).
(224) Sambur, J. B.; Chen, P. Distinguishing Direct and Indirect Photoelectrocatalytic Oxidation Mechanisms Using Quantitative Single-Molecule Reaction Imaging and Photocurrent Measurements. *J. Phys. Chem. C* **2016**, *120*, 20668−20676.
(225) Zhang, J.; Nosaka, Y. Mechanism of the OH Radical Generation in Photocatalysis with TiO_2 of Different Crystalline Types. *J. Phys. Chem. C* **2014**, *118*, 10824−10832.
(226) Barbero, N.; Vione, D. Why Dyes Should Not Be Used to Test the Photocatalytic Activity of Semiconductor Oxides. *Environ. Sci. Technol.* **2016**, *50*, 2130−2131.
(227) Krumova, K.; Cosa, G. Fluorogenic Probes for Imaging Reactive Oxygen Species. In *Photochemistry*, Albini, A.; Fasani, E., Eds.; The Royal Society of Chemistry, 2013; Vol. *41*, pp 279−301.
(228) Li, X.; Gao, X.; Shi, W.; Ma, H. Design Strategies for Water-Soluble Small Molecular Chromogenic and Fluorogenic Probes. *Chem. Rev.* **2014**, *114*, 590−659.
(229) Marín-Hernández, C.; Toscani, A.; Sancenón, F.; Wilton-Ely, J. D. E. T.; Martínez-Máñez, R. Chromo-Fluorogenic Probes for Carbon Monoxide Detection. *Chem. Commun.* **2016**, *52*, 5902−5911.
(230) Zhang, J.; Yue, C.; Ke, Y.; Qu, H.; Zeng, L. Fluorescent Probes for the Detection of Biogenic Amines, Nitrite and Sulfite in Food: Progress, Challenges and Perspective. *Advanced Agrochem* **2023**, *2*, 127−141.
(231) Zhang, C.; Xie, H.; Zhan, T.; Zhang, J.; Chen, B.; Qian, Z.; Zhang, G.; Zhang, W.; Zhou, J. A New Mitochondrion Targetable Fluorescent Probe for Carbon Monoxide-Specific Detection and Live Cell Imaging. *Chem. Commun.* **2019**, *55*, 9444−9447.
(232) Wu, J.; Jiang, L.; Verwilst, P.; An, J.; Zeng, H.; Zeng, L.; Niu, G.; Kim, J. S. A Colorimetric and Fluorescent Lighting-up Sensor Based on ICT Coupled with PET for Rapid, Specific and Sensitive Detection of Nitrite in Food. *Chem. Commun.* **2019**, *55*, 9947−9950.
(233) Meng, Y.; Yuan, C.; Du, C.; Jia, K.; Liu, C.; Wang, K.-P.; Chen, S.; Hu, Z.-Q. A Coumarin-Based Portable Fluorescent Probe for Rapid Turn-on Detection of Amine Vapors. *Spectrochimica Acta Part A: Molecular and Biomolecular Spectroscopy* **2021**, *262*, 120152.
(234) Kaloo, M. A.; Raja Sekhar, A.; Ramana Reddy, R. V.; Raman, R. S.; Sankar, J. A Facile and Visual Approach for the Detection of Trace Level Ammonia Vapours under Ambient Conditions. *Journal of Materials Chemistry C* **2016**, *4*, 2452−2456.
(235) Li, C. W.; Ciston, J.; Kanan, M. W. Electroreduction of Carbon Monoxide to Liquid Fuel on Oxide-Derived Nanocrystalline Copper. *Nature* **2014**, *508*, 504−507.
(236) Dhara, K.; Lohar, S.; Patra, A.; Roy, P.; Saha, S. K.; Sadhukhan, G. C.; Chattopadhyay, P. A New Lysosome-Targetable Turn-on Fluorogenic Probe for Carbon Monoxide Imaging in Living Cells. *Anal. Chem.* **2018**, *90*, 2933−2938.
(237) Ma, Z.; Li, J.; Hu, X.; Cai, Z.; Dou, X. Ultrasensitive, Specific, and Rapid Fluorescence Turn-on Nitrite Sensor Enabled by Precisely Modulated Fluorophore Binding. *Advanced Science* **2020**, *7*, 2002991.
(238) Strobl, M.; Walcher, A.; Mayr, T.; Klimant, I.; Borisov, S. M. Trace Ammonia Sensors Based on Fluorescent near-Infrared-Emitting Aza-BODIPY Dyes. *Anal. Chem.* **2017**, *89*, 2859−2865.
(239) Iriawan, H.; Andersen, S. Z.; Zhang, X.; Comer, B. M.; Barrio, J.; Chen, P.; Medford, A. J.; Stephens, I. E. L.; Chorkendorff, I.; Shao-Horn, Y. Methods for Nitrogen Activation by Reduction and Oxidation. *Nature Reviews Methods Primers* **2021**, *1*, 56.
(240) Huang, P.-W.; Hatzell, M. C. Prospects and Good Experimental Practices for Photocatalytic Ammonia Synthesis. *Nat. Commun.* **2022**, *13*, 7908.
(241) Steinmiller, E. M. P.; Choi, K.-S. Photochemical Deposition of Cobalt-Based Oxygen Evolving Catalyst on a Semiconductor Photoanode for Solar Oxygen Production. *Proc. Natl. Acad. Sci. U. S. A.* **2009**, *106*, 20633−20636.
(242) Zhong, D. K.; Cornuz, M.; Sivula, K.; Gratzel, M.; Gamelin, D. R. Photo-Assisted Electrodeposition of Cobalt-Phosphate (Co-Pi) Catalyst on Hematite Photoanodes for Solar Water Oxidation. *Energy Environ. Sci.* **2011**, *4*, 1759−1764.
(243) Reece, S. Y.; Hamel, J. A.; Sung, K.; Jarvi, T. D.; Esswein, A. J.; Pijpers, J. J. H.; Nocera, D. G. Wireless Solar Water Splitting Using Silicon-Based Semiconductors and Earth-Abundant Catalysts. *Science* **2011**, *334*, 645−648.
(244) Li, R.; Zhang, F.; Wang, D.; Yang, J.; Li, M.; Zhu, J.; Zhou, X.; Han, H.; Li, C. Spatial Separation of Photogenerated Electrons and Holes among {010} and {110} Crystal Facets of $BiVO_4$. *Nat. Commun.* **2013**, *4*, 1432.
(245) Shaner, M. R.; McKone, J. R.; Gray, H. B.; Lewis, N. S. Functional Integration of Ni-Mo Electrocatalysts with Si Microwire Array Photocathodes to Simultaneously Achieve High Fill Factors and Light-Limited Photocurrent Densities for Solar-Driven Hydrogen Evolution. *Energy Environ. Sci.* **2015**, *8*, 2977−2984.
(246) Wenderich, K.; Mul, G. Methods, Mechanism, and Applications of Photodeposition in Photocatalysis: A Review. *Chem. Rev.* **2016**, *116*, 14587−14619.
(247) Hannagan, R. T.; Giannakakis, G.; Flytzani-Stephanopoulos, M.; Sykes, E. C. H. Single-Atom Alloy Catalysis. *Chem. Rev.* **2020**, *120*, 12044−12088.
(248) Gao, C.; Low, J.; Long, R.; Kong, T.; Zhu, J.; Xiong, Y. Heterogeneous Single-Atom Photocatalysts: Fundamentals and Applications. *Chem. Rev.* **2020**, *120*, 12175−12216.
(249) Zhang, F.; Zhu, Y.; Lin, Q.; Zhang, L.; Zhang, X.; Wang, H. Noble-Metal Single-Atoms in Thermocatalysis, Electrocatalysis, and Photocatalysis. *Energy Environ. Sci.* **2021**, *14*, 2954−3009.
(250) Peng, B.; Liu, H.; Liu, Z.; Duan, X.; Huang, Y. Toward Rational Design of Single-Atom Catalysts. *J. Phys. Chem. Lett.* **2021**, *12*, 2837−2847.
(251) Li, X.; Bi, W.; Zhang, L.; Tao, S.; Chu, W.; Zhang, Q.; Luo, Y.; Wu, C.; Xie, Y. Single-Atom Pt as Co-Catalyst for Enhanced Photocatalytic H_2 Evolution. *Adv. Mater.* **2016**, *28*, 2427−2431.

(252) Lee, B.-H.; Park, S.; Kim, M.; Sinha, A. K.; Lee, S. C.; Jung, E.; Chang, W. J.; Lee, K.-S.; Kim, J. H.; Cho, S.-P.; Kim, H.; Nam, K. T.; Hyeon, T. Reversible and Cooperative Photoactivation of Single-Atom Cu/TiO_2 Photocatalysts. *Nat. Mater.* **2019**, *18*, 620−626.
(253) Chen, Y.; Ji, S.; Sun, W.; Lei, Y.; Wang, Q.; Li, A.; Chen, W.; Zhou, G.; Zhang, Z.; Wang, Y.; Zheng, L.; Zhang, Q.; Gu, L.; Han, X.; Wang, D.; Li, Y. Engineering the Atomic Interface with Single Platinum Atoms for Enhanced Photocatalytic Hydrogen Production. *Angew. Chem., Int. Ed.* **2020**, *59*, 1295−1301.
(254) Zhang, L.; Long, R.; Zhang, Y.; Duan, D.; Xiong, Y.; Zhang, Y.; Bi, Y. Direct Observation of Dynamic Bond Evolution in Single-Atom Pt/C_3N_4 Catalysts. *Angew. Chem., Int. Ed.* **2020**, *59*, 6224−6229.
(255) Chen, J.; Iyemperumal, S. K.; Fenton, T.; Carl, A.; Grimm, R.; Li, G.; Deskins, N. A. Synergy between Defects, Photoexcited Electrons, and Supported Single Atom Catalysts for CO_2 Reduction. *ACS Catal.* **2018**, *8*, 10464−10478.
(256) Gao, C.; Chen, S.; Wang, Y.; Wang, J.; Zheng, X.; Zhu, J.; Song, L.; Zhang, W.; Xiong, Y. Heterogeneous Single-Atom Catalyst for Visible-Light-Driven High-Turnover CO_2 Reduction: The Role of Electron Transfer. *Adv. Mater.* **2018**, *30*, 1704624.
(257) Yuan, L.; Hung, S.-F.; Tang, Z.-R.; Chen, H. M.; Xiong, Y.; Xu, Y.-J. Dynamic Evolution of Atomically Dispersed Cu Species for CO_2 Photoreduction to Solar Fuels. *ACS Catal.* **2019**, *9*, 4824−4833.
(258) Liu, S.; Yang, H. B.; Hung, S.-F.; Ding, J.; Cai, W.; Liu, L.; Gao, J.; Li, X.; Ren, X.; Kuang, Z.; Huang, Y.; Zhang, T.; Liu, B. Elucidating the Electrocatalytic CO_2 Reduction Reaction over a Model Single-Atom Nickel Catalyst. *Angew. Chem., Int. Ed.* **2020**, *59*, 798−803.
(259) Li, S.; Lu, X.; Zhao, S.; Ceccato, M.; Hu, X.-M.; Roldan, A.; Liu, M.; Daasbjerg, K. p-Block Indium Single-Atom Catalyst with Low-Coordinated In-N Motif for Enhanced Electrochemical CO_2 Reduction. *ACS Catal.* **2022**, *12*, 7386−7395.
(260) Liu, S.; Wang, Y.; Wang, S.; You, M.; Hong, S.; Wu, T.-S.; Soo, Y.-L.; Zhao, Z.; Jiang, G.; Qiu, J.; Wang, B.; Sun, Z. Photocatalytic Fixation of Nitrogen to Ammonia by Single Ru Atom Decorated TiO_2 Nanosheets. *ACS Sustainable Chem. Eng.* **2019**, *7*, 6813−6820.
(261) Han, L.; Liu, X.; Chen, J.; Lin, R.; Liu, H.; Lü, F.; Bak, S.; Liang, Z.; Zhao, S.; Stavitski, E.; Luo, J.; Adzic, R. R.; Xin, H. L. Atomically Dispersed Molybdenum Catalysts for Efficient Ambient Nitrogen Fixation. *Angew. Chem., Int. Ed.* **2019**, *58*, 2321−2325.
(262) Speck, F. D.; Paul, M. T. Y.; Ruiz-Zepeda, F.; Gatalo, M.; Kim, H.; Kwon, H. C.; Mayrhofer, K. J. J.; Choi, M.; Choi, C. H.; Hodnik, N.; Cherevko, S. Atomistic Insights into the Stability of Pt Single-Atom Electrocatalysts. *J. Am. Chem. Soc.* **2020**, *142*, 15496−15504.
(263) Feng, K.; Zhang, H.; Gao, J.; Xu, J.; Dong, Y.; Kang, Z.; Zhong, J. Single Atoms or Not? The Limitation of EXAFS. *Appl. Phys. Lett.* **2020**, *116*, 191903.
(264) Guo, Y.; Siretanu, I.; Zhang, Y.; Mei, B.; Li, X.; Mugele, F.; Huang, H.; Mul, G. pH-Dependence in Facet-Selective Photo-Deposition of Metals and Metal Oxides on Semiconductor Particles. *Journal of Materials Chemistry A* **2018**, *6*, 7500−7508.
(265) Chen, R.; Pang, S.; An, H.; Zhu, J.; Ye, S.; Gao, Y.; Fan, F.; Li, C. Charge Separation Via Asymmetric Illumination in Photocatalytic Cu_2O Particles. *Nature Energy* **2018**, *3*, 655−663.
(266) Rossi, L. M.; Fiorio, J. L.; Garcia, M. A. S.; Ferraz, C. P. The Role and Fate of Capping Ligands in Colloidally Prepared Metal Nanoparticle Catalysts. *Dalton Transactions* **2018**, *47*, 5889−5915.
(267) Amit, E.; Dery, L.; Dery, S.; Kim, S.; Roy, A.; Hu, Q.; Gutkin, V.; Eisenberg, H.; Stein, T.; Mandler, D.; Dean Toste, F.; Gross, E. Electrochemical Deposition of N-Heterocyclic Carbene Monolayers on Metal Surfaces. *Nat. Commun.* **2020**, *11*, 5714.
(268) Wang, M.; Yang, Y.; Shen, J.; Jiang, J.; Sun, L. Visible-Light-Absorbing Semiconductor/Molecular Catalyst Hybrid Photoelectrodes for H_2 or O_2 Evolution: Recent Advances and Challenges. *Sustainable Energy & Fuels* **2017**, *1*, 1641−1663.
(269) Bae, S.; Jang, J.-E.; Lee, H.-W.; Ryu, J. Tailored Assembly of Molecular Water Oxidation Catalysts on Photoelectrodes for Artificial Photosynthesis. *Eur. J. Inorg. Chem.* **2019**, *2019*, 2040−2057.
(270) Liang, X.; Cao, X.; Sun, W.; Ding, Y. Recent Progress in Visible Light Driven Water Oxidation Using Semiconductors Coupled with Molecular Catalysts. *ChemCatChem.* **2019**, *11*, 6190−6202.
(271) Wadsworth, B. L.; Khusnutdinova, D.; Moore, G. F. Polymeric Coatings for Applications in Electrocatalytic and Photoelectrosynthetic Fuel Production. *Journal of Materials Chemistry A* **2018**, *6*, 21654−21665.
(272) Yashas, S. R.; Shahmoradi, B.; Wantala, K.; Shivaraju, H. P. Potentiality of Polymer Nanocomposites for Sustainable Environmental Applications: A Review of Recent Advances. *Polymer* **2021**, *233*, 124184.
(273) Soucy, T. L.; Dean, W. S.; Zhou, J.; Rivera Cruz, K. E.; McCrory, C. C. L. Considering the Influence of Polymer-Catalyst Interactions on the Chemical Microenvironment of Electrocatalysts for the CO_2 Reduction Reaction. *Acc. Chem. Res.* **2022**, *55*, 252−261.

https://doi.org/10.1021/cbmi.3c00075
Chem. Biomed. Imaging 2023, 1, 692−715